Measuring stress-strain behavior of mild steel at intermediate strain rates

D.A. van Leeuwen

Thesis for the degree of MSc in Marine Technology in the specialization of track Science - Structures

Measuring stress-strain behavior of mild steel at intermediate strain rates

by

D.A. van Leeuwen

Performed at

Technische Universiteit Delft

Date of Exam
4 March 2022

This thesis MT.21/22.015 M is classified as confidential in accordance with the general conditions for projects performed by the TUDelft.

Supervisor
Responsible supervisor: Dr. C.L. Walters
E- mail: C.L.Walters@tudelft.nl

Thesis exam committee
Chair/Responsible professor: Dr. C.L. Walters
Staff member: Dr.Ir. X. Jiang
Staff member: M. Adly, MSc.

Author details Study
number: 4523628

TUDelft

Acknowledgements

Abstract

Impacts on offshore installations and ships can cause strains at high rates. It is known that mild steel lower yield stress and hardening are strain rate dependent. Measuring this material behavior is not easy, as test results from many researchers, show heavy vibration. Vibration is normally referred to as ringing. This thesis aims at measuring stress-strain behavior of mild steel at intermediate strain rates between 100 s^{-1} and 500 s^{-1} with minimal vibration. Two major characteristics from stress-strain behavior in this research, are the lower yield stress and plastic tangent modulus.

A comparison of public test results, showed a steel characteristic for transferring quasi-static stresses, to stresses at a desired strain rate. This characteristic has been used to transfer a quasi-static stress-strain curve to stress-strain curves at intermediate strain rates. This strain rate dependent material model is used in calculations. The test is modelled by means of an explicit finite element analysis. The analysis showed that adding a plastic hinge in the specimen, can reduce bending and vibration.

The test setup is a drop tower, where the drop weight falls into a U-shaped specimen. Strains are measured in an elastically and plastically deforming area on the specimen. Stresses in the plastic area can be obtained from strains in the elastically deforming area. Strains are measured by means of digital image correlation. Stresses are compared with loads obtained from drop weight positions and consequent accelerations.

Measured plastic strains compare well to predicted plastic strains. However, stresses from first tests show vibration in a range of 20 percent of the average stress or more. If such bending occurs, it is not exactly known where the average stress is. However, the amount and direction of bending can be obtained from the 3D position measurements. The bending investigation is only used to identify causes of ringing.

With insight in bending and loads from two separate measurements, this test is considered to produce results that represent the material behavior of mild steel. A raw test result with a vibration range of 20 percent of the average stress, in the first test setup, shows the potential for obtaining raw measurements from a U-shaped specimen in a drop test.

Contents

List of Figures

List of Tables

1

Introduction

Collisions of ships can cause large plastic deformations in a short duration. This can cause a large strain rate, which is the time derivative of strain. Typical values for strain rates during a collision are $300s^{-1}$ to $500s^{-1}$, according to Huh et al., 2009. Nowadays it is possible to calculate how colliding structures will deform, with great level of detail. The calculation needs a material model as input. The behavior of mild steel is strain rate sensitive. In order to model a ship collision, a strain rate dependent material model is needed.

Measuring strain rate dependent constitutive behavior is done on a large strain rate domain. A strain rate of $0.01s^{-1}$ is considered a quasi-static strain rate in this report. Publicly available test data also show strain rates over millions per second. There is an intermediate range of strain rates, where obtaining a stress-strain curve is difficult. This difficult range typically varies from intermediate strain rates of $100s^{-1}$ to $500s^{-1}$. The problem with testing material properties at intermediate strain rates is that the testing normally features vibrations, which could occur in translation or rotation. Many methods are used to process data with heavy ringing, as shown in the following examples. Getter et al., 2015 uses a modelled force signal as measurement. Huh et al., 2009 has used Fast Fourier Transform to remove frequency components above a certain frequency limit. The aim of this thesis is to measure strain rate dependent stress-strain behavior in a pure way, without filtering, smoothing. Therefore, the research question in this thesis is as follows.

How can mild steel stress-strain behavior be obtained at the intermediate strain rate?

Two main characteristics of stress-strain behavior are tangent modulus and lower yield strength. The answer on the main question is in measuring the two main characteristics. The test needs to be designed such, that smoothing or filtering test data is not necessary. Therefore, ringing needs to be minimized in the design phase. Tensile tests have been performed on many velocities, with many test setups as described by Bhujangrao et al., 2020. A typical test duration in this thesis is in the order of a millisecond. This is normally smaller than the response time of a servo-hydraulic test machine. Therefore, a drop tower is used. A drop tower has been designed and manufactured in this thesis. Using a drop tower and digital image correlation provides the opportunity to obtain the load both from drop weight accelerations and from elastic strain in the specimen. A drop tower creates a compressive impact. Therefore, the compression needs to be transferred into a tensile loading in the specimen. A U-shaped specimen is a simple and light weight solution. Light weight is important, as ringing is reduced by reducing masses that need to be accelerated, as done by Xia et al., 2016 and Zhu et al., 2011. Removing conventional load cell and it's mass from the test setup, avoids an important source of ringing. The idea of the U-shaped specimen is first presented by Chan, 2009. Later, it is considered by others, Perogamvros et al., 2016 and Broekhuis, 2020. The U-shaped specimen has not yet been physically tested. The concept test setup is as follows.

The specimen with its components is shown in figure 1.1, together with the reference coordinate system. Inside a conventional load cell, an elastic deformation of the steel core is measured by means of strain gauges and correlated to a static load, prior to a test. In a comparable way, there is an elastically deforming section in the specimen, which is filmed by high speed cameras. Elastic deformations are obtained from the recordings by means of 3-dimensional digital image correlation. This provides the load on the gauge section. The gauge section deformation is recorded at the same time.
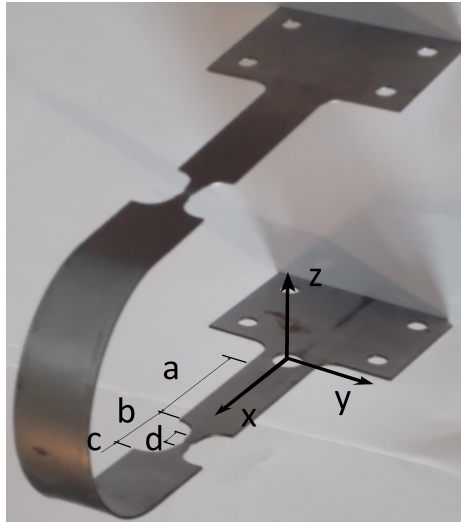
Figure 1.1: Reference coordinate system and specimen components, a: clamp section, b: distance between shoulders, c: catcher, d: gauge section

Figure 1.2 shows conceptual drop tower components. The drop weight slides between 2 guiding beams. The only degree of freedom of the drop weight is a translation in x-direction. by letting the end of the specimen's clamp section be part of the guiding beams, there is minimal clearance between drop weight and specimen. This reduces bending vibration during the test.

(a) Drop weight

(b) One guiding beam of the drop tower

(c) Drop weight, guiding beam and a specimen

Figure 1.2: Conceptual drop tower components

The setup is designed such, that the drop weight fits inside the specimen and the drop tower, with a clearance of 0.2mm. Figure 1.3 shows the complete drop tower and how the drop weight fits inside the specimen at the moment of impact. The drop tower stands on two legs, because the cameras are positioned close to the specimen and need to be able to film the specimen from different angles. There needs to be a powerful light source as well.
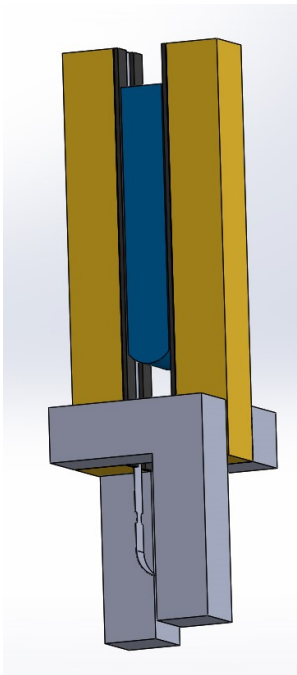
(a) Complete drop tower
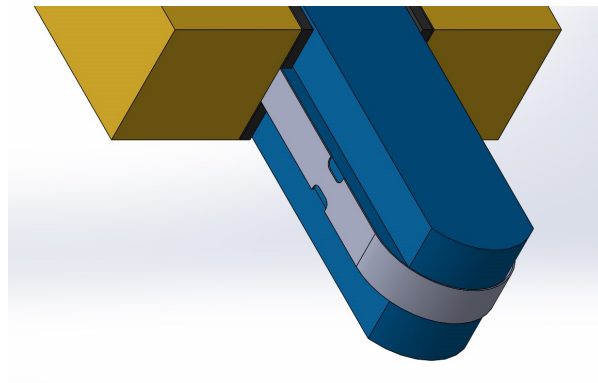
(b) The drop weight fits exactly inside the specimen

Figure 1.3: Compete drop tower and structural detail

In order to present measurements from the physical test, the method of obtaining the strain rate needs to be defined. This is done in chapter 2. This definition is used in calculations as well. The specimen is designed by means of an explicit finite element analysis, with the aim at a measurable stress-strain curve. This analysis needs a strain rate dependent material model. The strain rate dependent material model is determined in chapter 3. The initial test parameters are obtained from a preliminary calculation in chapter 4. This calculation is also used to check the finite element model in chapter 5. Initial test parameters are iterated further through different design steps in chapter 6, by means of the explicit method. The physical outcome is the test setup as presented in chapter 7. Experimental results are shown in chapter 8. The discussion of the results is described in chapter 9 and conclusions in chapter 10.

2

Strain rate assessment

Work of many researchers show several different definitions of strain rate during a test. A choice of strain rate definition affects the one-dimensional simulation in chapter 4 and presentation of results in chapter 8. Therefore, a definition is chosen in this chapter. There is no standard method yet, for obtaining strain rate during testing. Having a standard method, makes results better comparable.

During a typical dynamic tensile test, strain energy is transferred into the specimen. If an impactor is used, the velocity of an impactor is reduced. This reduces strain rate during the test. Strain rate is defined as the time derivative of strain, $\dot{\epsilon} = d\epsilon/dt$. Fang, 2021 uses Forward Euler in post processing his digital image correlation measurement, as shown in the following equation. The equation shows that the derivative is calculated per time step. A time derivative in a simulation and measurement can be very rough. A typical picture is shown below in figure 2.1. This signal shows too much non-physical oscillation to determine the strain rate from during the simulation. Therefore, this method is not used in the calculation or to characterise a complete test result.

$$\dot{\epsilon}_n = \frac{\epsilon_{n+1} - \epsilon_n}{t_{n+1} - t_n} \tag{2.1}$$
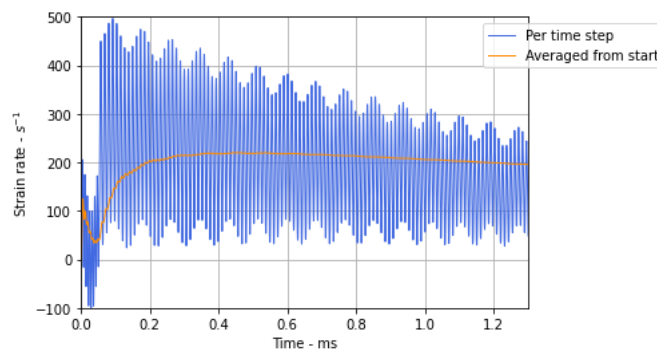
Figure 2.1: Typical strain rate per time step in the equation of motion in chapter 4

The strain increment over the time difference is another definition of strain rate. This equals integrating strain rate over time, divided by the duration. Finally, the average strain rate can be obtained from integrating the strain rate over strain. This equation is also used in conjunction with principal strains. However, the considered strains in this project are presented until necking. Therefore, the principal strain is nearly equal to ϵ_{11} in this project. The integral of equation 2.2 is based on the graph in figure 2.2.

$$\dot{\epsilon}_{avg} = \frac{1}{\epsilon_{end}} \int \dot{\epsilon} d\epsilon \tag{2.2}$$

5
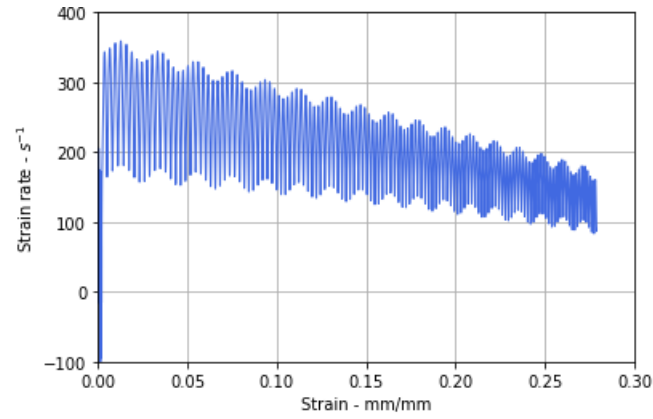
Figure 2.2: Strain rate as function of strain

The choice of strain rate definition affects calculations in chapter 4. In a simulation, the actual gauge section stress is compared with the lower yield stress. If the lower yield stress is reached in a certain time step, the gauge section starts to yield. Effects of different strain rate definitions in that simulation influence the yield stress as shown in table 2.1. The difference in strain rate is significant. The lower yield stress differs by more than 10 percent. The effect of the choice between integral over time and integral over strain is also shown in figure 2.3. The different lines are obtained from different definitions in the simulation. The first slope is the elastic region and the second slope is the first part of the plastic strain domain, which follows the expected initial plastic strain rate. Only when yielding, the initial yielding strain rate increases to an expected value close to $\dot{\epsilon} = V/L_0$.

Table 2.1: Different methods of average strain rate assessment in the elastic portion of the simulation

Average strain rate	$\frac{1}{t_{max}}\int \dot{\epsilon}\, dt$	$\frac{1}{\epsilon_{max}}\int \dot{\epsilon}\, d\epsilon$
Strain rate at lower yield - s^{-1}	39	145
Lower yield stress - MPa	388	427
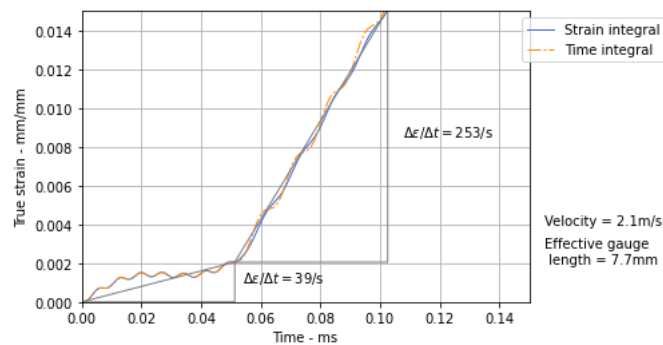
Figure 2.3: Different strain rate definitions in a simulation

The strain rate definition does not influence the simulation, until the lower yield point. The time integral represents the best strain rate over this duration, from zero until the yield point, as that value equals $\Delta\epsilon/\Delta t$. The gauge section strain rate before yielding is that low, because no specimen section is yielding yet. Therefore each section takes a significant portion of the drop weight displacement. The low value of the strain rate is representative for the pre-yielding strain rate in the gauge section. This is the rate that the lower yield stress should be based on. Therefore the strain rate integral over time is chosen for calculations.

3

Material model

A material model directly influences specimen design. For example, the deformation of the clamp section depends directly on the load on the gauge section. This connection is made by the material model. The simulations used for specimen design, need a strain rate dependent material model as input. The material model is also used to put physical measurements of this thesis into perspective. It is a check whether measurements can make sense. A common and simple strain rate sensitivity model is compared with publicly available test results.

Strain rate sensitivity is presented by many researchers per steel type. It is often presented as a stress-strain rate curve. It is normally presented on logarithmic or half-logarithmic scale. For demonstrating linear lines on logarithmic scale, the data are presented on logarithmic scale in this thesis as well. A comparison between different research has not been found yet. Therefore, the work of 8 researchers is compared here. The group of researchers is as follows: Huh et al., 2009, Langseth et al., 1991, Jocham et al., 2017, Singh et al., 2013, Pipard et al., 2013, Xia et al., 2015, Fang, 2021 and Scholl et al., 2018. Figure 3.1 shows lower yield stresses as function of strain rate. Figure 3.2 shows ultimate stresses as function of strain rate.
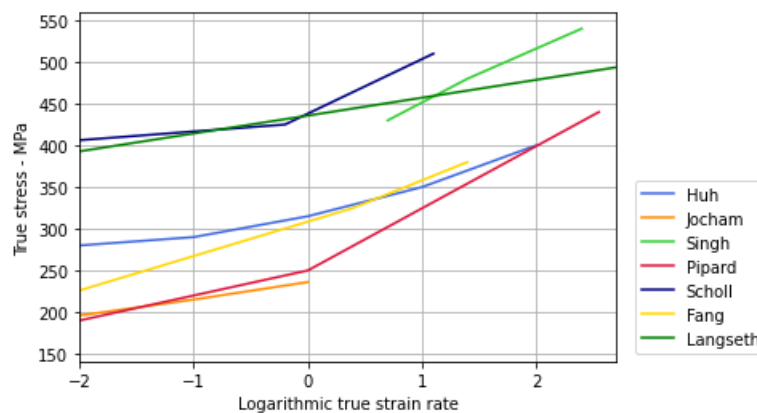
Figure 3.1: Strain rate effects on lower yield stresses by Huh et al., 2009, Jocham et al., 2017, Singh et al., 2013, Pipard et al., 2013, Scholl et al., 2018, Fang, 2021, Langseth et al., 1991
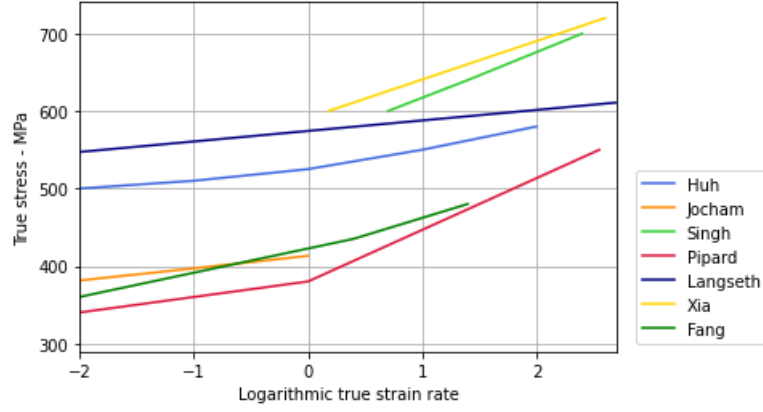
Figure 3.2: Strain rate effects on ultimate stresses by Huh et al., 2009, Jocham et al., 2017, Singh et al., 2013, Pipard et al., 2013, Xia et al., 2015, Fang, 2021, Langseth et al., 1991

Figures 3.1 and 3.2 show what kind of stress increment to expect when strain rate is increased. Also, an envelope of experimental stresses can be drawn. This will be used in later comparisons. The envelope shows the stress range over the strain domain. Therefore, the highest ultimate stress line and the lowest lower yield line are taken to form the envelope. In general, lower yield stresses show larger slopes than ultimate stresses. This means, as concluded by the majority of the researchers, that lower yield stress behaves more strain rate sensitive than ultimate stresses and hardening decreases with strain rate. These effects need to be captured in the strain rate sensitivity model to be chosen in this thesis.

3.1. Public strain rate sensitivity results and Cowper-Symonds

The work of 8 researchers is compared with a common relatively simple strain rate sensitivity model. This is the model from Cowper and Symonds, 1957 as shown in equation 3.1, where σ_t is true stress. D and q are material dependent parameters. The comparison is shown in figure 3.3. Table 3.1 shows examples of values for the parameters in the Cowper-Symonds equation.

$$\sigma_{t_{dynamic}} = \sigma_{t_{static}} \left(1 + \left(\frac{\dot{\epsilon}}{D} \right)^{1/q} \right) \tag{3.1}$$

Table 3.1: Comparison of common values for the Cowper-Symonds equation and values that compare to statistics

Parameter	Cowper-Symonds	Values in this thesis	Unit
D	40.4	808	s^{-1}
q	5	5	-
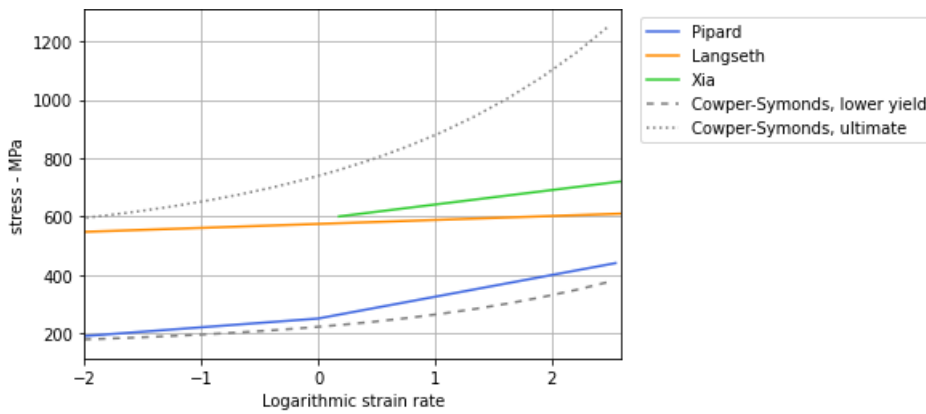
Figure 3.3: The envelope of public research compared with Cowper- Symonds equation and values

The intermediate strain rates in this thesis range from 100 s^{-1} to 500 s^{-1}. That is the logarithmic domain between 2 and 2.7. At that domain, it can be seen that Cowper-Symonds over estimates the stress by roughly 80 percent. Therefore, the Cowper-Symonds parameters are adjusted for a better fit. Variation of q does not improve the result. Adjustment of D as shown in table 3.1, shows the result in figure 3.4. The over-estimation is still in the order of 25 percent or roughly 200 MPa in that domain.
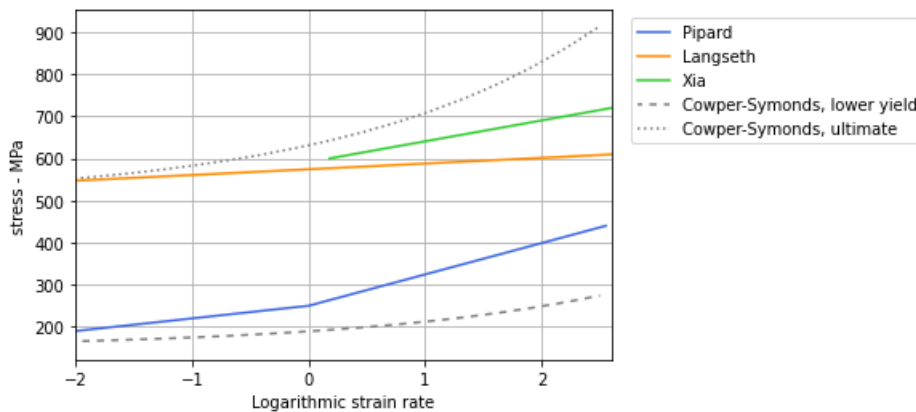
Figure 3.4: The envelope of public research compared with Cowper- Symonds equation and adjusted values

An over-estimation of 25 percent of the load in the gauge section, causes the cross-sectional area of the clamp section to be 25 percent too large. That means less deformation in the clamp section. Measuring the small elastic clamp deformation is a challenge, during the test in this thesis. The over-estimation of 25 percent needs to be avoided. Therefore, the analyses of other strain rate sensitivity researchers is investigated. Researchers keep concluding that strain hardening does not increase with strain rate Langseth et al., 1991, Huh et al., 2009. This phenomenon is to be included in the newly developed material model.

3.2. Strain rate sensitivity model

The aim of this section is to find a model with significantly lower deviation from public data than the Cowper-Symonds strain rate sensitivity model. The lines from different researchers as shown in figures 3.1 and 3.2, at the start of this chapter, are considered to create a uniform direction field. This is not the case, as some lines do intersect on domain $-2 \leq \log \dot{\epsilon} \leq 2.7$. However, the angles between lines are small. The largest deviation from the considered research will be presented. A general formula is established, for lines in the direction field. The formula is obtained from lines presented by Fang, 2021, who presented two straight lines through a data set, shown in figure 3.5.
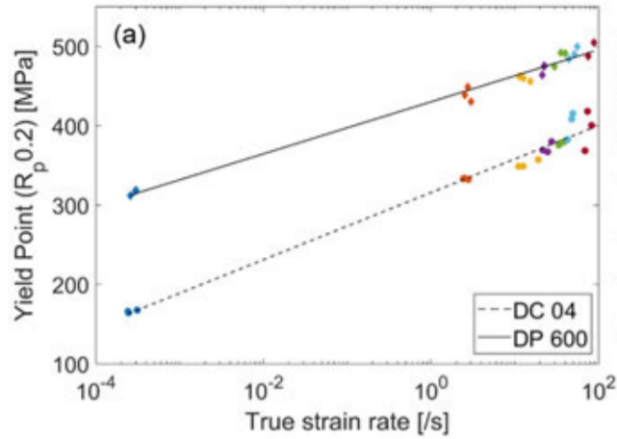
Figure 3.5: Linear exponential stress-strain rate results by Fang, 2021

The slope of the lines through the data points is slowly reducing with increasing stress. If it is assumed that the slope reduces proportionally to increasing quasi-static stress, the relation can be used to calculate a dynamic stress from a quasi-static stress at any strain rate. The equation is as follows, where x is the logarithmic strain rate, y is true stress. The quasi-static stress y_0 is transferred to a dynamic stress $y(x)$. This model is referred to as linear exponential strain rate sensitivity model. The slope difference $\partial\partial y/\partial x\partial y$ is obtained from both presented lines. The difference between the lowest presented line and the quasi-static stress to be transferred is Δy. The slope of the lowest line is $\left(\frac{\partial y}{\partial x}\right)_0$.

$$y(x) = \left(\left(\frac{\partial y}{\partial x}\right)_0 + \frac{\partial\partial y}{\partial x\partial y}\Delta y\right) x + y_0 \tag{3.2}$$

This equation is used to create the lines in figure 3.6. The public data lines are in the intermediate strain rate domain and or give the largest deviation from the linear exponential strain rate sensitivity model. As can be seen in the picture, the difference with the Langseth results are largest. The largest deviation is less than 100 MPa. This is less than half the deviation of the Cowper-Symonds strain rate sensitivity model. The comparison whith the envelop of public data is shown in figure 3.7.
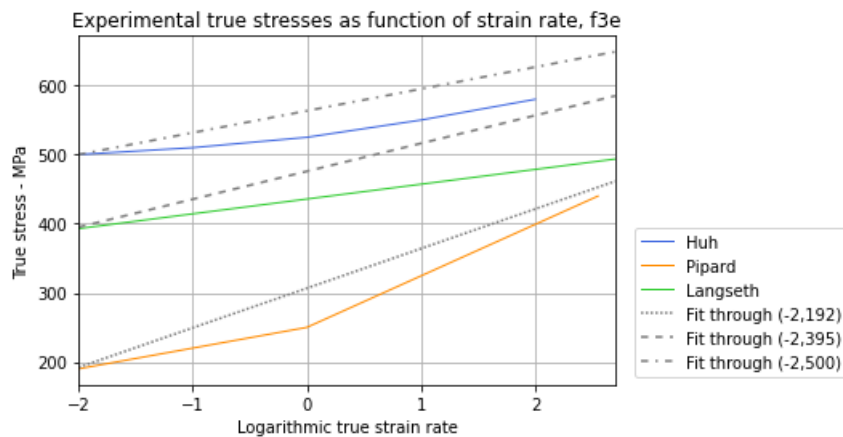
Figure 3.6: Comparison of the linear exponential strain rate sensitivity model and public data
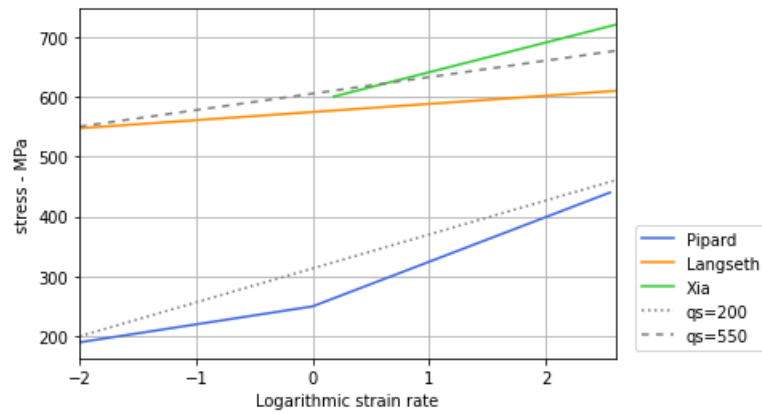
Figure 3.7: Comparison of the linear exponential strain rate sensitivity model with public data envelope

The linear exponential strain rate sensitivity model is used to transfer a quasi-static stress-strain curve point by point to dynamic stress-strain curves. The result is shown in figure 3.8. The quasi-static stress-strain curve is obtained from Huh et al., 2009. This is the result for SPRC390E-bh steel that shows common lower yield stress and ultimate stress values.
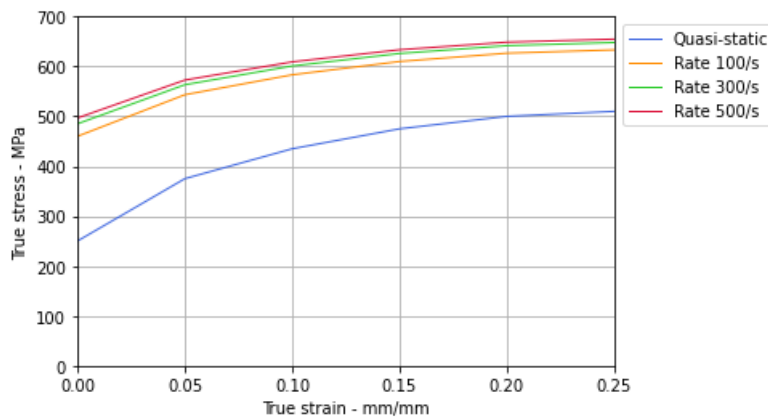
Figure 3.8: Material model from the linear exponential strain rate sensitivity model, the input for further calculations

Chronologically, the specimen was designed prior to the literature survey. The design is therefore based on an initial material model. This is a bi-linear strain rate dependent material model, based on Cowper-Symonds. Based on the linear exponential strain rate sensitivity model, the clamp width had been adjusted, as the gauge load was 25 percent lower than the Cowper-Symonds estimation. The design outcomes have also been checked with the linear exponential strain rate sensitivity model. From the check, it followed that the main design considerations remained the same. The linear exponential strain rate sensitivity model is compared with an own developed parabolic exponential strain rate sensitivity model. This model had a slightly larger deviation than the linear one. Therefore the linear model is shown here. The parabolic model is shown explained in appendix B. The resulting stress-strain curve is nearly equal to the stress-strain curves obtained from the linear model.

<div align="right">4</div>

One-dimensional simulation

The test specimen can be designed such, that the behavior in the measured sections is quasi-one-dimensional. That is useful, because the drop test is a material test. It is also convenient to compare behavior from finite element analysis from Abaqus with calculations. Calculations are referred to as one-dimensional numerical solution of the equation of motion. This is one-dimensional solution for short. Calculations are also used to investigate strain rate reduction by dimensions of specimen components. The one-dimensional solution behaves comparable to the Abaqus solution, it is used for parametric studies as well. By the end of this chapter, there is one-dimensional explicit finite element analysis.

Specimen behavior can be modelled by an initial value problem. The equation of motion is as follows, where m is the drop weight mass. The values are shown in table 4.1. All cases in this chapter are calculated with the same initial velocity v_0. In the 1-element calculation, only scalars are used in the equation of motion. In the 3-element calculation, the boldface components are vectors. Both 1 and 3-element configurations are shown in figure 4.1.
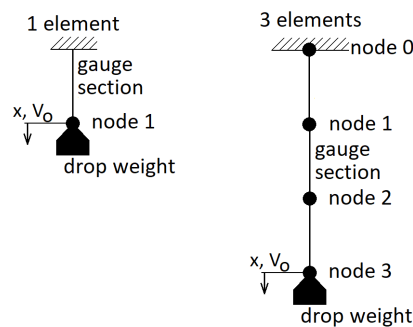
Figure 4.1: Free body diagrams for different calculations

Table 4.1: Parameters in the equation of motion

Parameter	Value	Unit
Initial velocity, v_0	1.4	m/s
Effective gauge length, L	7.6	mm
Damping, d	0.5	N/s
Stiffness, k	$AE/L = 385$	MN/m
Mass, m	12.5	kg

$$m\ddot{\mathbf{x}} + d\dot{\mathbf{x}} + k\mathbf{x} = mg \tag{4.1}$$

The equation of motion is transferred to the following set of linear equations.

$$\dot{x}_1 = x_2 \tag{4.2}$$

$$\dot{\mathbf{x}}_2 = -m^{-1}\, k\, \mathbf{x}_1 - m^{-1}\, d\, \mathbf{x}_2 + g \tag{4.3}$$

The system is solved numerically, as shown in the following equation. This procedure is similar to $\ddot{\mathbf{x}} = m^{-1}\mathbf{f}$, where $\mathbf{f}$ is the sum of internal and external forces, by Schutte et al., 2010. A first order time integration method causes the script to become very slow as the solution starts to converge from millions of time steps. Therefore, Runge Kutta 4 is chosen. Runge Kutta 4 is an explicit time integration method for initial value problems. Still, 10000 time steps are required for convergence of the strain solution to within one percent deviation from the converged value.

$$\dot{\mathbf{x}} = \begin{bmatrix} 0 & I \\ -m^{-1}\,k & -m^{-1}\,d \end{bmatrix} \mathbf{x} + \begin{bmatrix} 0 \\ -g \end{bmatrix} \tag{4.4}$$

Solving the system of equations, leads to the following displacements and strain as pictured in figure 4.2. Where k is a scalar. This solution is useful for obtaining initial test setup parameters. A test at an intermediate strain rate up to 500 s^{-1} requires a non-zero initial velocity, if practicable specimen dimensions are used. The maximum gauge length is in the order of a centimeter, if the drop tower fits in a normal room. However, it does not show what is going on in the gauge section exactly. The initial part of the displacement graph does not show much more than the free fall of the drop weight. This is a reason to include more specimen sections in the simulation.

(a) Displacement (b) Stress-strain curve
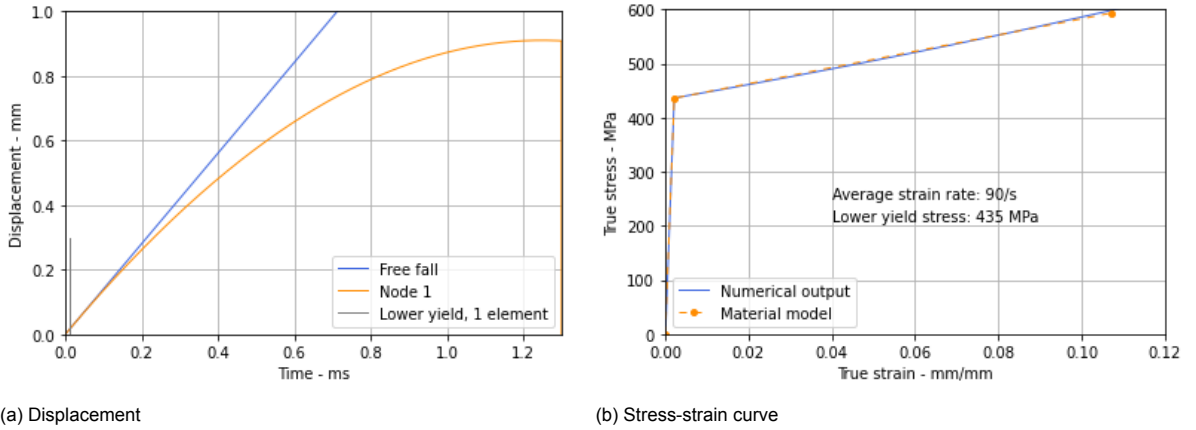
Figure 4.2: Numerical solution of the equation of motion, 1 element

The gauge section radii reduce the strain rate slightly. The gauge section length in one-dimensional solutions is the gauge section length plus the portion between the radii that deviates less than 5 percent from the gauge width. In case of a gauge length of 5 mm and a radius of 7 mm, this results in an effective gauge length of 7.6mm.

Instead of solving the equation of motion for one element, three elements are now considered. This creates an opportunity to study consequences of the elastic regime or simulate a sliding clamp. The elements are the clamp and gauge section and the catcher. Each section is modelled as a linear one-dimensional bar element, with a start node and an end node. This gives the following equilibrium equations in the specimen.

$$f_1 = k_1 u_1 - k_1 u_2$$
$$f_2 = -k_1 u_1 + (k_1 + k_2)u_2 - k_2 u_3 \tag{4.5}$$
$$f_3 = -k_2 u_2 + (k_2 + k_3)u_3 - k_3 u_4$$
$$f_4 = -k_3 u_3 + k_3 u_4$$

This system is written as $\mathbf{f} = K\mathbf{u}$. Term $K\mathbf{u}$ is substituted in the equation of motion. In the numerical scheme, K is a 4 by 4 stiffness matrix. Mass matrix m is a 4 by 4 diagonal matrix, containing the masses of the specimen sections and the drop mass on the fourth node. Damping matrix d is also a diagonal matrix. I is an identity matrix. The material model developed in chapter 3.2 is used. The strain rate dependent stress-strain curve is interpolated between zero strain and 0.1 mm/mm. If the lower yield stress is exceeded in an element, it gets the reduced stiffness as the slope of the stress-strain curve in the yield domain is lower than the elastic strain domain. The element force of the yielding element is however higher than the elastic force. Therefore, the element force at the moment of switching from elastic to plastic regime, is added to the element force as a constant in the yield strain domain.

In order to be able to present a stress-strain curve from the 3-element solution, material damping is used. Xia et al., 2016 report a value for damping ratio D between 0.1 and 0.8 N/s. This includes a specimen with fixture and load cell. The value for D is chosen to be 0.5 in the one-dimensional simulation. This gives the strain results, as presented in this chapter. The one-dimensional 3-element configuration is shown in 4.3. The purpose of both sets of pictures is to investigate how much the geometry of the specimen components influences the strain rate. The gauge section displacement shows a small difference between one specimen element or 3 specimen elements.

(a) Displacements

(b) Stress-strain curve
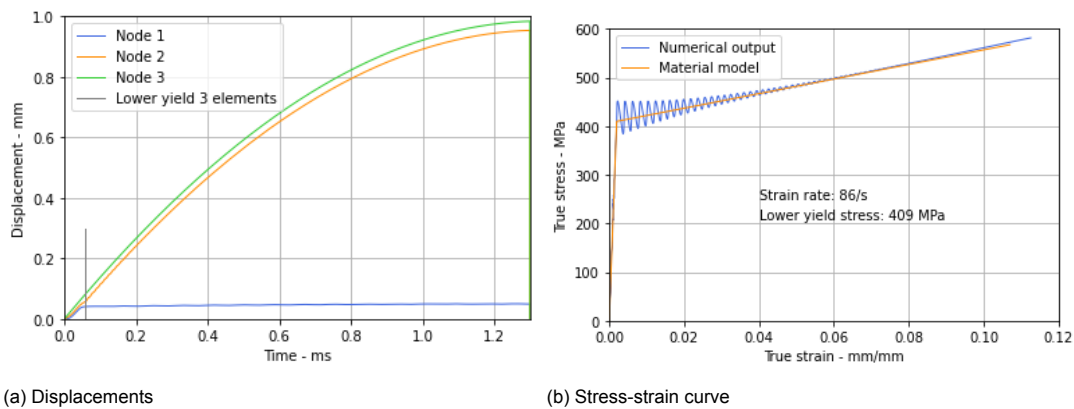
Figure 4.3: Numerical solution of the equation of motion, 3 elements

The one-element calculation directly follows the expectation with respect to the strain rate in the elastic part of the strain domain. The strain rate should equal $v/L_0 = 184s^{-1}$, where it is 185 s^{-1}. As the specimen does not break in this case, the strain rate drops to zero. This gives the average strain rate of 90 s^{-1}. The initial derivative of the displacement superimposes on the initial velocity of the drop mass. The three-element solution has a comparable average strain rate.

The strain histories of the one and three-element simulations are shown in figure 4.4. When the gauge section behaves elastically, the drop weight displacement is distributed over the three components. Therefore, the initial strain rate is low. This behavior is an important difference between the one-element and 3-element configuration. Only if the gauge section starts to yield, nearly all further drop weight displacement results in strain in the gauge section. Just after yielding, the strain rate is as expected from $\epsilon = \dot{V}_0/L_0$. The delayed yield of the gauge section and deflection of the other elements, only cause a strain rate reduction of roughly 5 percent.
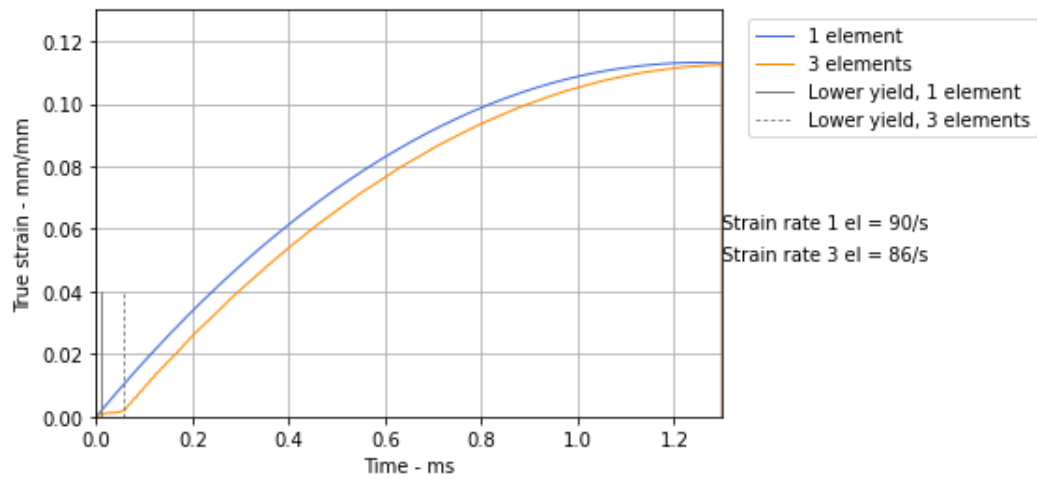
Figure 4.4: Gauge section strain histories from derivation with different numbers of elements

Solving the equation of motion for one element in one dimension, gave understanding in some major test parameters, such as drop mass and initial velocity. This has been used in choosing the test setup. Solving the equation of motion for three elements will be compared to the commercial finite element analysis and the model validation by means of a physical test. When used in a parameter study, solving the equation of motion in one dimension saves a considerable amount of time. The 3 element configuration helped in understanding the reduction in strain rate, caused by the catcher, clamp section and radii.

5

Finite Element Analysis

A three-dimensional explicit finite element analysis model is used in Dassault Systèmes Abaqus 2020 Student edition, referred to as Abaqus. The explicit method is already described in chapter 4 as a common way to solve the equation of motion. Initial test parameters from design 1 are obtained from the one-dimensional simulation in chapter 4. The specimen will be designed for minimal bending and longitudinal vibration. Shell elements can bend about 3 axes. Therefore, the shell element is chosen. Only the U-shape is modelled first, there is no cut-out yet for the dog bone shapes of the legs of the U. The minimum number of elements, needed for convergence, gives an impression how many elements are needed in the the catcher and the clamp section. The U-shape already converged from 108 elements. The specimen and drop weight with mesh and boundary conditions are shown in figure 5.1a. The drop weight is an analytic rigid surface. It is shown with an offset in y-direction to make a clear distinction. The picture shows the mesh with 108 elements. A courser mesh is not considered necessary. Convergence is shown in figure 5.2a. Test parameters are shown in table 5.1. Boundary conditions don't go well together with contact surfaces. Therefore, the complete U-shape is modelled. Both ends of the U are restricted in all 6 degrees of freedom. The drop weight has 5 restricted degrees of freedom. The only permitted drop weight translation, is in x-direction.

Table 5.1: Test parameters Design 1

	Drop mass	Velocity	Width	Leg length	Catcher radius	Gauge length	Gauge width	Dog bone radius
	kg	m/s	mm	mm	mm	mm	mm	mm
U-shape only	30	4	30	100	50			
U-shape with dog bone	30	4	30	100	50	10	5	5
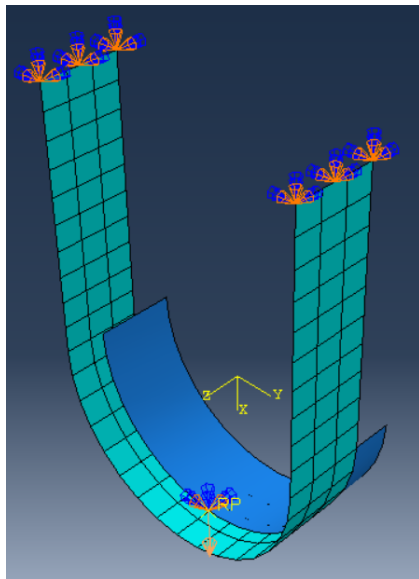
(a) Drop weight and specimen with mesh and boundary conditions
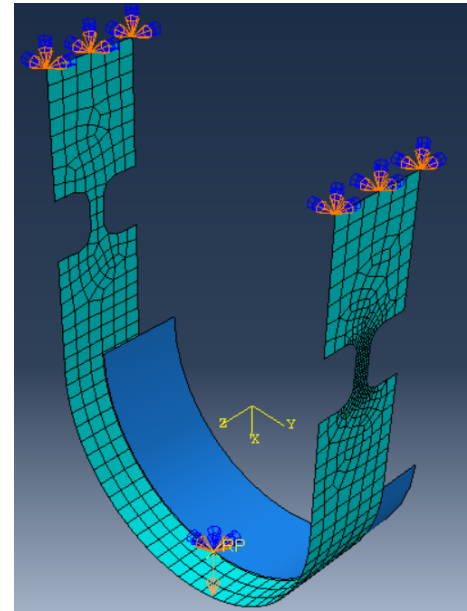
(b) U-shaped specimen with dog bone details

Figure 5.1: Global mesh and local details

Finally, the complete U-shape is modelled with the dog bone-shaped legs. Local mesh refinements are applied for convergence of the solution. With a ratio of 1:2 for element length or width to thickness, the deviation is still below one percent Abaqus, 2017. This aspect ratio is encountered in the finest mesh. Convergence is checked in strain signals, as strain is the primary digital image correlation outcome. Stress and strain are the last outputs to converge from a finite element analysis. Figure 5.2b shows how strains in the gauge section have converged over the complete time domain. Abaqus results show good agreement with the one-dimensional simulation from chapter 4. A reason for the small difference, is that the one-dimensional simulation uses a bi-linear material model.

The number of integration points through thickness did not make a difference for the U-shaped specimen geometry with respect to the average gauge section stress. Four integration points in the shell element are used. The number of output time steps are based on the highest expected vibration frequencies. Abaqus takes time steps based on the sound wave velocity in the material and the smallest mesh size, Abaqus, 2017.
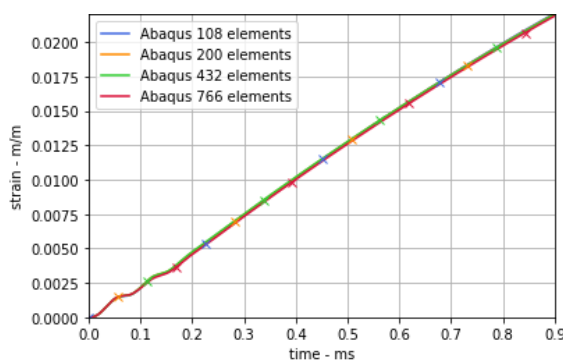
(a) Convergence of the U-shape without structural details
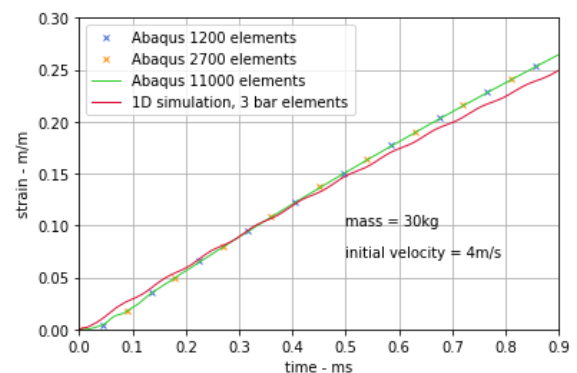
(b) Model validation by convergence and comparison

Figure 5.2: Global and local convergence

6

Test design

This chapter mainly shows specimen design considerations. The specimen is designed for minimal unwanted effects, bending and longitudinal vibration. Specimen design 1, the U-shape with dog-bone shaped legs from chapter 5 is investigated for bending of gauge and clamp section, in chapter 6.1. Varying geometrical parameters leads to Specimen design 2 in chapter 6.2. A geometrical feature needs to be added to reduce unwanted effects, as shown in chapter 6.3. A material model update leads to an alteration of the clamp section in chapter 6.4. The specimen designs are shown in table 6.1. The identities of different specimen designs refer to iterations. The added feature in the specimen design is only meaningful if the investigation of Specimen design 2 is described. This is an example why the design steps have been described. As the clamp strain signal still shows unwanted effects, a second method of obtaining the gauge section load is considered in chapter 6.5. Post processing is setup in chapter 6.6. This is relevant for the physical test results. It is also relevant for how the stress-strain curves are presented per specimen design, as if they were measured in the physical experiment. A final factor that influences test setup design, is resolution of the cameras, as shown in chapter 6.7.

Table 6.1: Specimen designs

Specimen design							
	Clamp		Gauge			Catcher	
	Length	Width	Length	Width	Radius	Width	Radius
	mm	mm	mm	mm	mm	mm	mm
Specimen design 1	100	30	10	5	5	30	50
Specimen design 2	200	20	10	5	5	35	50
Specimen design 3	90	20	5	5	7	25	50
Specimen design 4	90	15	5	5	7	25	50

6.1. Bending investigation Specimen design 1

Specimen bending influences the strain measurements in x-direction, referred to as normal strain. Bending is found in the gauge section and clamp section. It is caused by restricted contraction by the drop weight and stretching a curved portion of the specimen. As the normal strain in the gauge section is high, a small bending moment creates a relatively small deviation on the strain measurement as pictured below in figure 6.1a. Relative bending strain is obtained by dividing the strain on the front side by the strain on the backside of one half of the U-shape, as can be seen in equation 6.1. This is done per integration point. Only minimum and maximum relative bending strains from all the integration points are presented over time. Relative bending is a convenient criterion for the parameter study, as it includes normal and bending strain in one number. Bending strain in itself is not a design criterion. However, the bending strain itself will also be presented, as it is used together with the normal strain to compare the design iterations. Gauge section bending is below 4 percent, which means that the

bending strain is lower than 2 percent of the normal strain.

$$\epsilon_R = \frac{\epsilon_{front}}{\epsilon_{back}} \tag{6.1}$$
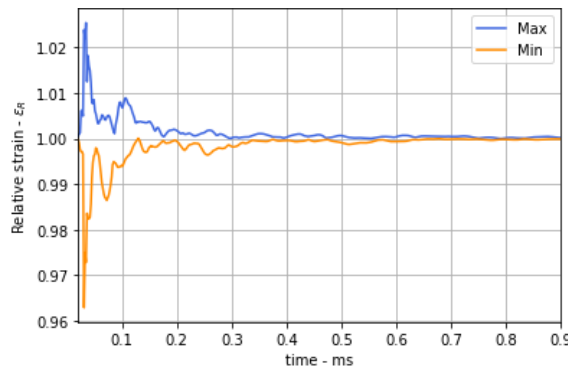
(a) Relative bending, gauge section elements of one half of the U-shape
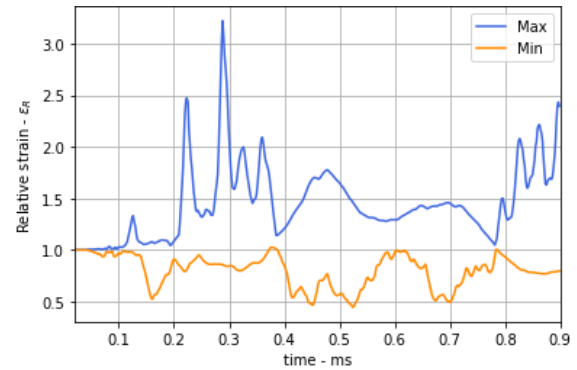
(b) Relative bending, clamp section elements of one half of the U-shape

Figure 6.1: Bending in different sections

Strains in the clamp section, where the force is measured, need to be in the elastic domain. That means that clamp strains are in the order of a factor 100 lower than the gauge section strains. In that case, the same bending moment that was insignificant previously, becomes significant in the clamp section as shown in picture 6.1b below. This is a problem, as strain is measured on the specimen surface on one side. The other side of the gauge section is invisible, because of the drop weight. A relative strain difference of front and backside of nearly 400 percent is shown. That means that the bending strain difference is much larger than the normal strain. This renders the optical strain measurement useless. This is the reason that a bending minimization is carried out in the next section.
Figures 6.2a and 6.2b show strains in the clamp section. Both bending and longitudinal vibration are significantly present. The bending strain has nearly the same magnitude as the normal strain. Longitudinal vibration is much smaller than bending, but still significant. The normal strain has been obtained from averaging the strains in x-direction in the clamp section, for both sides of the clamp section. This is a global clamp section value. In agreement with the relative bending procedure, bending strain is a local value from one integration point. Bending strain is obtained by subtracting the normal strain from the strain in x-direction on the surface of one side of the clamp section.
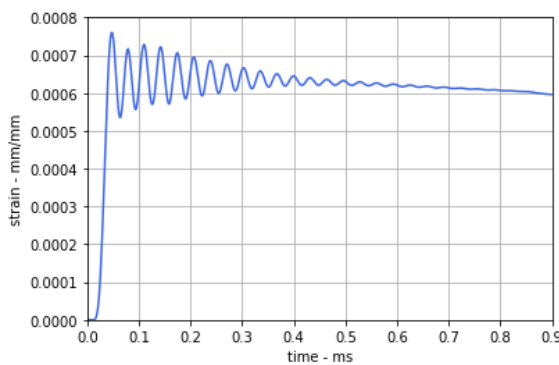
(a) Clamp, normal strain
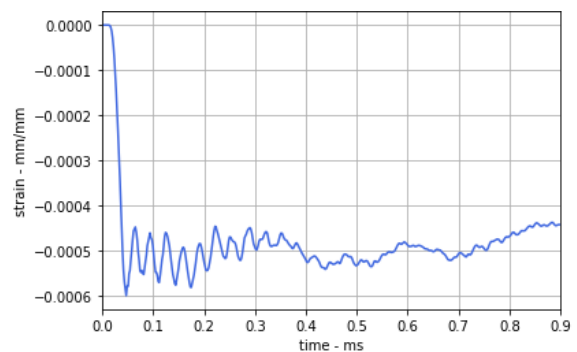
(b) Clamp, bending strain

Figure 6.2: Specimen design 1

6.2. Bending minimization, Specimen design 2

Dog bone and U-shape dimensions are varied in order to see how bending is minimized. Design 1, presented in table 5.1, is input for this paragraph. This paragraph leads to Design 2. The table below shows a large improvement with increasing clamp section length. The clamp length of 200 mm is taken for further design. This length is considered an upper boundary for the clamp length, as a sufficient portion of the drop weight needs to be guided in the drop tower during the test.

Table 6.2: Clamp length variation

Length [mm]	60	80	100	200
Relative bending range [-]	5	5	4	0.9

Table 6.2 shows values for the complete clamp section. The effect of the gauge section position on the clamp section is determined, results are shown in table 6.3. The gauge section cannot touch the catcher radius anyway, because the catcher radius needs a small run-out for physical production of the radius, either by rolling or pressing. Adjusting the gauge section position, reduces the bending by more than 50 percent. The gauge section deforms plastically, nearly during the complete test duration. Therefore it is a plastic hinge. At the location of the plastic hinge, the bending moment is zero. So, the location of the gauge section is varied over the clamp length. The position at 30 mm from where the catcher radius starts, shows the least bending. The position is measured from the catcher end to the gauge section centre.

Table 6.3: Gauge section position variation

centre position from radius[mm]	20	30	40	50	60
Relative bending range [-]	0.30	0.27	0.30	0.35	0.50

The strained catcher that looses contact with the drop weight is stretched. This causes a bending moment. The lower the strain in the catcher radius, the lower the length of curved material that is stretched. Therefore the catcher section is given a larger width in order to minimize bending. The effect of width variation is small. Catcher width 35 mm is chosen, see table 6.4. The radius of the drophead has also been varied. The result is shown below in table 6.5.

Table 6.4: Catcher width variation

Catcher width[mm]	25	30	35	40	45
Relative bending range [-]	0.24	0.24	0.21	0.23	0.23

Table 6.5: Drop head radius variation

Drophead radius[mm]	40	45	50	55	60
Relative bending range [-]	0.40	0.35	0.23	0.26	0.25

Increasing specimen thickness, increased bending significantly. This can be explained by the increased required moment to stretch the curved section that looses contact with the drop head. In addition, there is more asymmetric contraction. Also, the clamp length had a more detailed variation. This did not lead to better results. The minimization lead to clamp bending as shown below in figure 6.3. Compared to the initial design, the bending range went from 400 percent to 30 percent. The specimen dimensions from the first optimization are summarized in table 6.1.
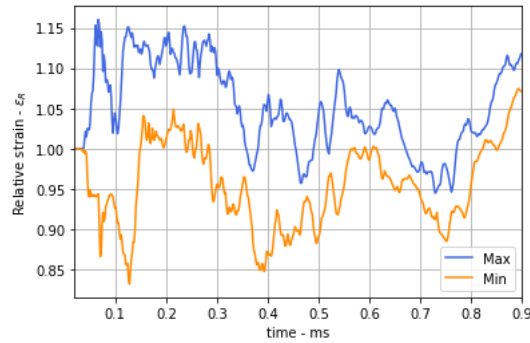
Figure 6.3: Relative bending, clamp section elements of one half of the U-shape, Specimen design 2

The bending minimization in this paragraph has reduced bending strain from 600μ to 80μ, as shown in figure 6.4b. This is a considerable improvement. However, on a target strain of 1000μ, this still creates an error of 8 percent. This is reflected by the relative bending strain of 16 percent in figure 6.3. Meanwhile, longitudinal vibration has worsened from an initial relative oscillation of 33 percent to 50 percent in Specimen design 2. This is a reason for adding a geometrical feature to the specimen.

(a) Clamp section normal strain

(b) Clamp section bending strain
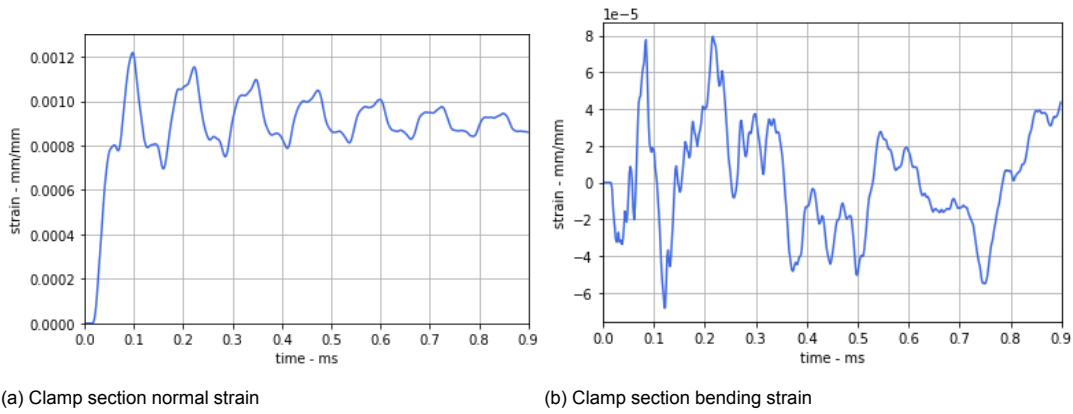
Figure 6.4: Specimen design 2

6.3. Specimen design 3, a new geometry

In order to isolate the clamp section from bending, the moment line over the clamp section length needs to be zero. This can be done by creating a clamp section between plastic hinges. Per definition, a hinge cannot transfer a bending moment. So, between plastic hinges, the bending moment line in this geometry will be close to zero. An extra plastic hinge is created by cutting a hole in the clamp section near the fixture. The specimen is shown in figure 6.5.
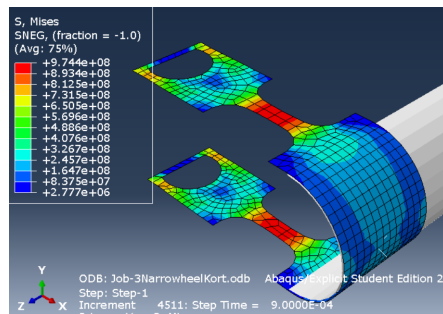
Figure 6.5: Clamp section between plastic hinges

The intended added plastic hinge has reduced bending. The longitudinal vibration seems to have

disappeared as well. Is it possible that a plastic area absorbs vibration? According to stress wave theory as described by Kolsky, 1964, stress waves travel with the speed of sound in the material. The speed of sound is dependent on the tangent modulus. When yielding, the tangent modulus can get small. Therefore, the velocity of a reflected stress wave gets small. So, reflected stress waves can be found in a plastically deforming area, but they will fade. Fang, 2021, also used a hole in the specimen to absorb vibration. So, besides reducing bending, a plastic hinge also absorbs longitudinal vibration.

The clamp section with a hole was an improvement for the smoothness of the stress-strain curve. However, the strain distribution in the clamp was so rough due to stress concentrations, that it is investigated what happened with a longer clamp and lower drop velocity. If the velocity is reduced by a factor, the gauge length needs to be reduced by the same factor, in order to maintain the desired strain rate. Therefore, the gauge length went from $10mm$ to $5mm$. When the ratio of gauge length and width was 5:1, the resulting strain rate was 400 per second, with a drop velocity of 4 m/s. Strain results for different ratios are shown in figure 6.6a, at a velocity of 2 m/s. When a gauge length to width ratio of 5:1 was used, the resulting stress strain curve was dramatic as shown in figure 6.6b.

(a) Strain histories for different gauge widths

(b) Stress-strain curves from element stress and stress 'as if measured'
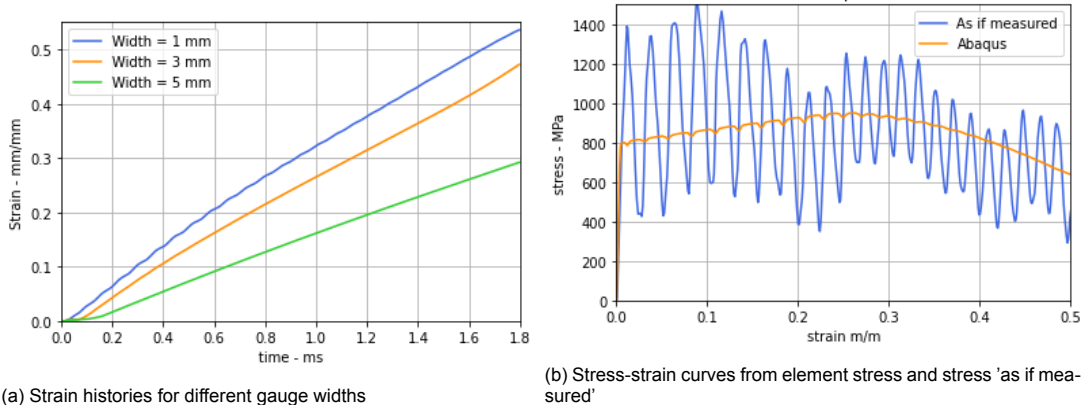
Also manufacturing and handling a specimen with length to width ratio of 5:1 is not advantageous for the test. This geometry was not considered practicable. It is easily damaged by handling and the stress-strain curve showed heavy vibration. Another option was to take the gauge length equal to the width, ratio 1:1. The gauge length and width were 5 mm. The result is as follows. The normal stress shows an insignificant vibration in figure 6.7a. Bending strain is larger than Specimen design 2, because of the smaller clamp length, as shown in figure 6.7b.

(a) Clamp secion normal strain

(b) Clamp section bending strain
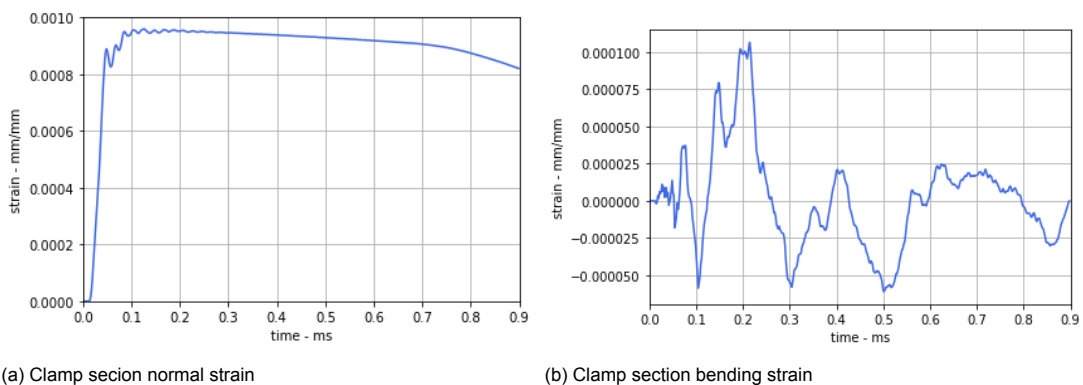
Figure 6.7: Specimen design 3

A comparison of clamp section strains is shown in figure 6.8a. The total strain on the surface, which will be captured by the camera, is the sum of bending and normal strain. Specimen design 1 has a bending strain in the same order of magnitude of the normal strain. On the surface, that means that constant bending can cancel out the normal stress. Specimen design 2 shows severe ringing on the

target strain. Specimen design 3 is chosen for further work, as it shows less ringing than specimen 2. Specimen design 3 shows more bending than Specimen design 2. At first glance, this is surprising, as Specimen design 3 has the added plastic hinge. However, Specimen design 3 has less than half the clamp length of Specimen design 2. As shown in the parameter study in table 6.2, this would cause a relative bending strain of 5. The bending strain is 'only' 10 percent of the normal strain. Therefore, the relative bending is 1.2, slightly higher than the bending of Specimen Design 2. The reduction of relative bending from 5 to 1.2 is primarily the effect of the added plastic hinge. The next step is to check the resulting stress-strain curve which is shown in figure 6.8b. The final specimen dimensions are shown in table 6.1.
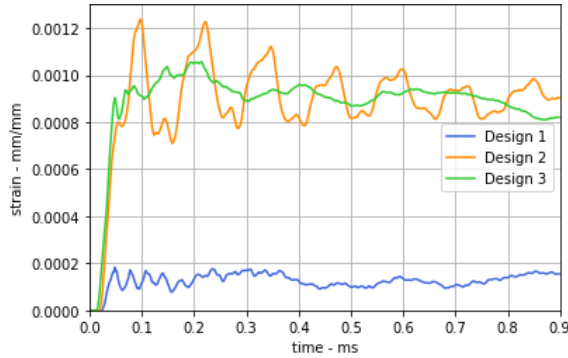
(a) Strain as if measured on the clamp surface: bending + normal strain
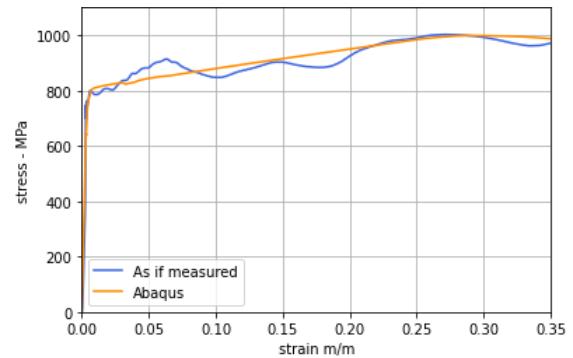
(b) Final stress-strain curve as if measured in the physical experiment

6.4. Specimen design 4

By the time that Specimen design 3 was finished, the literature survey was finished as well. An important finding of the literature survey was the own developed strain rate sensitivity model, explained in chapter 3.2. The new model has a smaller difference between the lower yield stress at low strain rate and the ultimate stress at the highest intermediate strain rate. Therefore, a smaller force is required to break the specimen, than estimated by Cowper-Symonds. This reduces the load and therefore the strain in the clamp section. The clamp deformation needs to be as large as possible in order to be able to capture the deformation by camera. With the new ratio between lowest lower yield and highest ultimate load, the clamp width had been adjusted from 20 to 15mm.

6.5. Force from positions

Another option to avoid the clamp with it's bending, is to mark the drop weight. The drop weight positions can be captured just besides the gauge section. From the drop weight acceleration, the force on the gauge section can be calculated. The resulting force signal is shown in figure 6.9. The force from the drop weight acceleration is equal to the element force.
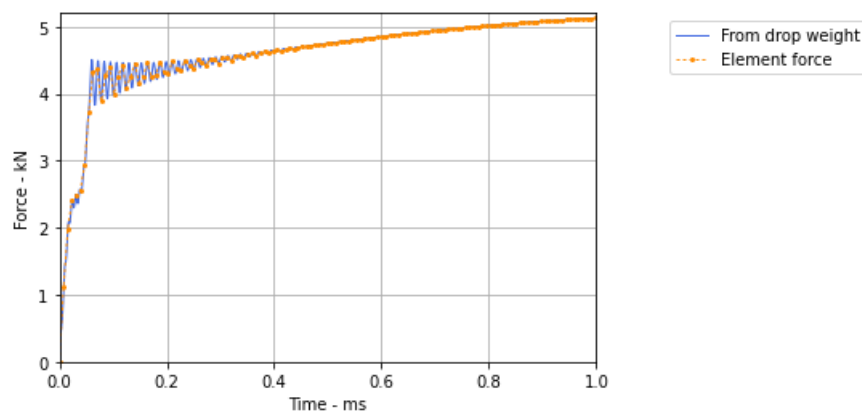
Figure 6.9: Element force compared with force from drop weight acceleration

6.6. Post processing

Stress in the gauge section is obtained from strain in the clamp section. The clamp section strain remains elastic. Therefore, the relation between clamp strain and load, is the Young's modulus and the clamp cross-sectional area. The clamp load is equal to the gauge load. In the gauge stress determination, the area as function of time is considered. The area as function of time is determined, based on conservation of volume.

$$F_{clamp}(t) = \epsilon(t)_{true} E A_{clamp}(t) \tag{6.2}$$

The cross-sectional area as function of time is obtained from the gauge volume that remains constant through the test period: $A(t)L(t) = A_0 L_0$. This leads to the following equation, which is used both in the clamp an gauge section.

$$A(t) = A_0 \frac{L_0}{L(t)} = \frac{A_0}{e^{\epsilon_{true}(t)}} \tag{6.3}$$

The resulting gauge section true stress is calculated as follows.

$$\sigma_{t_{gauge}}(t) = \frac{F_{clamp}(t)}{A_{gauge}(t)} \tag{6.4}$$

6.7. Resolution

Digital image correlation is developed in 1980's. For this thesis, digital image correlation is considered a black box that generates a position field of the specimen. However, some properties that influence specimen design, are described here. The filmed sections of the specimen have a speckle pattern. From the resolution per selected frame rate, the number of pixels over the section length is known. The preferred speckle size is 3 pixels. The algorithm tracks a unique set of speckles on a specified length. If the uniqueness of the speckle pattern is recognised, it can be counted how many pixels the set displaces and deforms. This is not only done on pixel scale. Gray shades used, so set positions can be interpolated between pixels. This increases the precision of the measurements by 50 times or better, according to Reedlunn et al., 2013. In the worst case, the precision would be the pixel size, divided by 50. The measurement accuracy provides 30 load levels in the stress-strain curve, as can be seen in table 6.6.

Table 6.6: Capturing a small displacement with 900 pixels in x-direction

Section	Length	maximum strain	Elongation	Measurement accuracy, 1 pixel = 0.1mm	Number of displecement steps
	mm	mm/mm	mm	mm	-
Clamp	60	0.001	0.06	0.002	30
Gauge	5	0.3	1.5	0.002	750

Movement of the specimen or drop weight during taking a picture causes blur in the picture. This is referred to as motion blurring, which needs to be avoided by adjusting the shutter time per frame. The maximum permissible motion during opening of the lens per picture is 0.1 pixel. With a pixel size of 0.1mm, this leads to a maximum motion per frame of 0.01mm. Consequences for the shutter time are shown in table 6.7. The table shows that the maximum shutter time is a quarter frame period. As a powerful light source is available, a tenth of the frame period is used.

Table 6.7: Shutter time at frame rate 50k fps

Velocity	Motion per frame	Shutter time	Motion per shutter opening
m/s	mm	frame duration	mm
2	0.04	1/4	0.01

<div style="text-align: right;">

7

</div>

<div style="text-align: right;">

Test setup

</div>

This chapter provides an overview of physical test parameters. All tests have been executed at room temperature. First, test parameters are shown per specimen. It is shown which information is obtained from digital image correlation for post processing. Finally, it is shown how the concept test setup design relates to reality. Table 7.1 shows specimens and their test parameters.

Table 7.1: Specimen test parameters

Specimen	Drop mass	Fall height	Frame rate	Resolution x-direction
	kg	cm	fps * 1000	pixels
5	4.5	25	50	896
6	4.5	25	20	1024
7	4.5	25	50	896
8	12.5	22	50	896
9	12.5	22	50	896

From specimen 5, it was observed that the resulting stress-strain curve had more than enough data points. Therefore, the frame rate had been reduced to 20000 frames per second, in order to increase the resolution for specimen 6. With increasing resolution, a projected pixel on the specimen gets smaller. Therefore, the pixel size needs to be reduced. In other words, the specimen needs to have a finer speckle pattern. The same calibration of specimen 5 had been used for specimen 6. The software could not correlate the results from specimen 6. Three dimensional positions are obtained from Istra4D v4.4.7x64. The grid of points is shown in figure 7.1. The black dots are locations where positions are obtained during a test. The clamp section has 12 points and the gauge section 10 points.
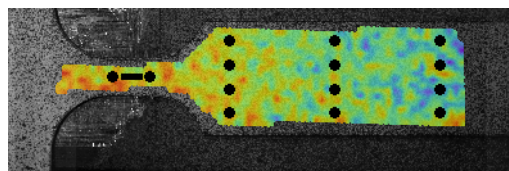
Figure 7.1: Locations where positions are obtained, during a test

The specimen is filmed by means of two Photron Fastcam SA-Z cameras. Points on the surface can be tracked in 3D space. Therefore, a speckle pattern is applied on the specimen. The speckle pattern is shown in figure 7.2. Ideally, the speckle size is 3 by 3 pixels. As can be seen in the picture, some speckles have the required size.

<div style="text-align: center;">

27

</div>
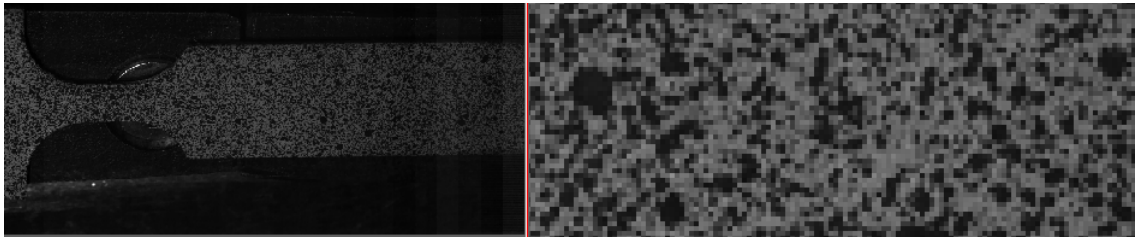
Figure 7.2: Speckle pattern on specimen 7

The first drop weight of 4.5 kg had an alignment error and was replaced by a machined drop weight of 12.5 kg. The concept structural detail in figure 1.3b is identical to the physical structural detail in figure 7.3a and 7.3b. Figure 7.4 shows how clearance between drop tower and drop weight is measured. The clearance between drop tower and specimen is less than 0.2 mm.

(a) Drop weight almost touches the catcher

(b) Drop weight touches the catcher

Figure 7.3: Drop weight and specimen

Figure 7.4: Clearance between drop tower and drop weight
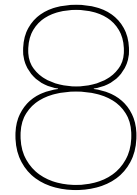
Test Results

Physical tests results are described in this chapter. Gauge section strains are considered in section 8.1. Drop weight motion is considered as loads are obtained from the drop weight positions in chapter 8.2. Together with loads derived from the clamp strain, this leads to stress-strain curves in chapter 8.3. Finally, the precision data from the digital image correlation software is checked in chapter 8.4.

8.1. Strain in the gauge section

If all specimen sections deform elastically, the strain rate in the gauge section is low. As soon as the gauge section starts to yield, the other sections almost stop deforming any further. Therefore all further drop weight displacement is transferred into strain in the gauge section. So, from the lower yield point, the strain rate in the gauge section increases as expected from $\dot{\epsilon} = V_0/L_0$. This increase in strain took place at a later moment in time, than expected. A reason for a late yield point, can be a lower yield stress, that turns out to be higher than expected. In this test, the clamp section shifted about 0.07mm in x-direction. This is significant if the specimen displacements have the same order of magnitude at that moment in time. Clamp section x-motion is shown in the picture below. The ramp in x-direction is used as boundary condition in the one-dimensional simulation. The results are shown below. All gauge section strains are shown in figure 8.2. The strain rates per specimen are shown in table 8.1. The time difference is taken from $t = 0$ to the first time record where the strain is larger than 0.25 mm/mm. Specimen 8 and 9 show the highest average strain rate over time. This corresponds with the drop weight that does not reach zero speed. Specimen 8 starts to strain earlier than the others. Possibly the specimen shifted less in the fixture.

(a) Clamp section x-displacements

(b) Gauge section strain, measured and calculated
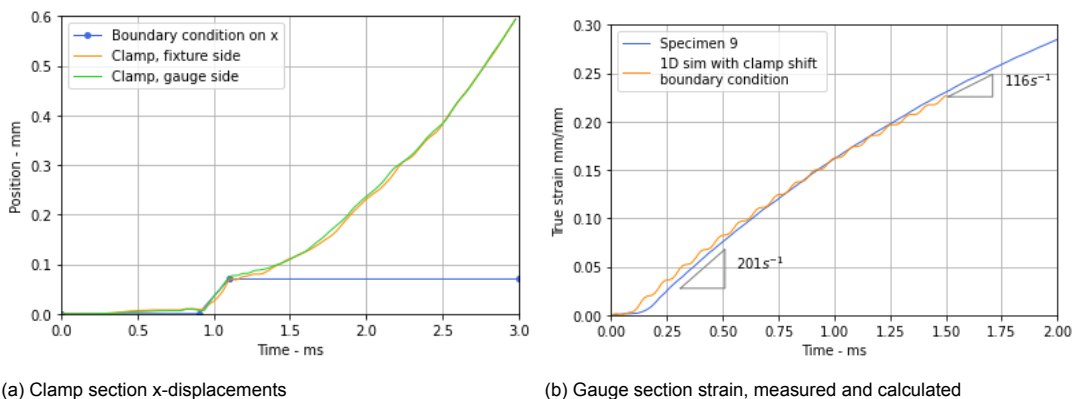
Figure 8.1: Gauge section strains and the reason for the late yield point, found clamp rigid body displacements
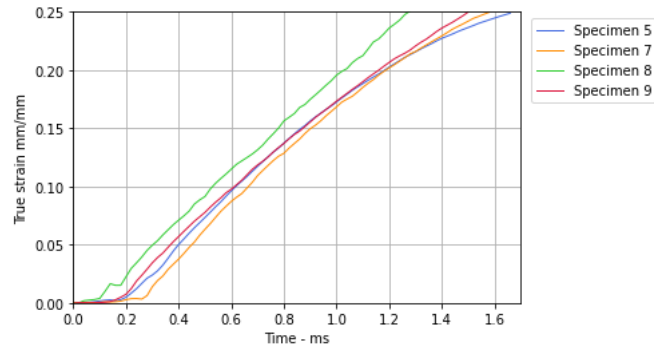
Figure 8.2: All gauge section strains

Table 8.1: Specimen strain rates

Specimen	Strain rate - s^{-1}
5	150
7	158
8	197
9	167

8.2. Load from drop weight acceleration

The drop weight has a speckle pattern. Three positions on the speckle pattern are monitored during the test. This provides complete three dimensional motion of the drop weight during each time step. The drop weight positions are shown below. Drop weight rotations are checked. For example, a small z-rotation, r_z, is obtained as follows, $r_z = -\partial y / \partial x$, where ∂x is the x-distance between two points and ∂y is the difference in y-displacement per time step. All three rotations are restricted by the drop tower. The clearance between drop tower and drop weight is measured prior to testing and is 0.2mm. With the drop weight still having 15 cm inside the drop tower, the maximum Y-rotation range is twice the clearance over the length: 0.003 radians. This compares to the measurements in figure 8.3. The signal is rough, due to very small displacement differences. Still, the rotations represent physical behavior.

(a) Drop weight positions

(b) Drop weight rotations
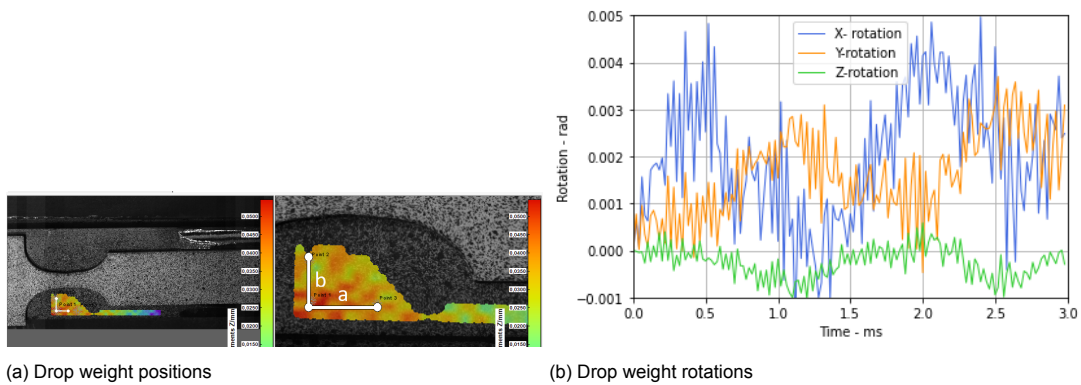
Figure 8.3: Drop weight positions and rotations

Specimen load is obtained from drop weight x-positions. The x-positions are shown in figure 8.4. The positions line is a very smooth line. Differentiating the line over 2 time steps, by means of the central difference formula, gives a very rough velocity curve. Therefore, the time step is chosen as $\Delta t = t_{n+\Delta n} - t_{n-\Delta n}$. Velocity curves for different Δn are presented in figure 8.4. The curve of $\Delta n = 8$, is smooth enough to differentiate a second time and still shows an average close to the curve of $\Delta n = 1$. The initial velocity is close to the intended initial velocity of 2.1 m/s. The difference is caused by friction. The increment in velocity, in the first millisecond, is nearly 0.01 m/s as expected from gravity. The fall

energy from the velocity difference is compared with the energy from the stress-strain curve integral with respect to strain. The energy from the velocity difference is 12.2 J in total. That is 6.1 J per half U.

(a) Drop weight x-positions, specimen 9   (b) Drop weight x-velocity
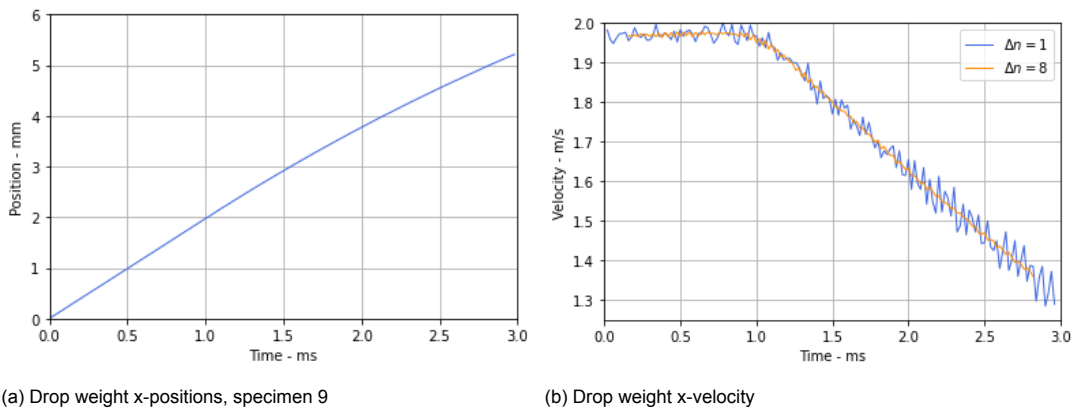
Figure 8.4: Drop weight positions and velocity

The velocity curve is differentiated with $\Delta n = 4$, in order to obtain the acceleration curve. By Newton's second law, this leads to the specimen load. This load acts on the reduced cross-sectional area of the specimen, which leads to the true stress, as described in chapter 6.6.

8.3. Stress-strain curves

Stress-strain results in this thesis are ideally presented until necking with the strain only obtained from longitudinal deformations. Figure 8.5 shows strains over the gauge length. The strains are obtained from 14 points over the inner 80 percent of the gauge section length. In the first millimeter, the strain does not rise anymore, if the strain is higher than 0.2 mm/mm. When the strain reaches 0.2mm/mm in the first millimeter, the average strain is 0.25mm/mm. Therefore, test results are presented up to 0.25 mm/mm.
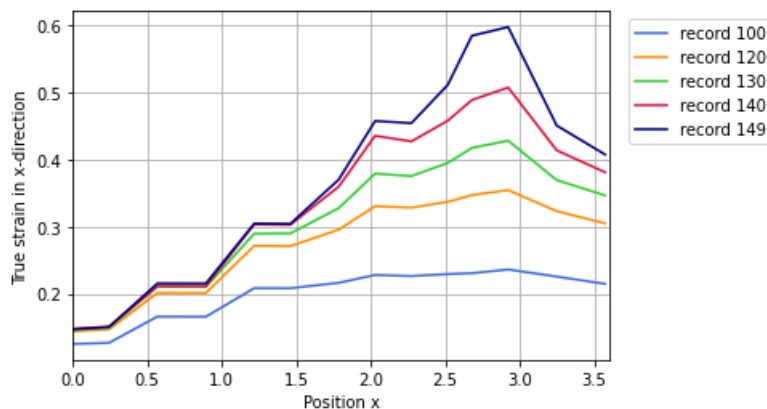
Figure 8.5: Strain distribution over gauge length

Strain rates per specimen over strain are conveniently comparable with stress-strain curves. The strain rates are shown in figure 8.6. The raw stress-strain curves, without bending compensation, are shown in figure 8.7 and 8.8. Specimen 5 shows the smallest range of ringing, roughly 20 percent of the stress magnitude.
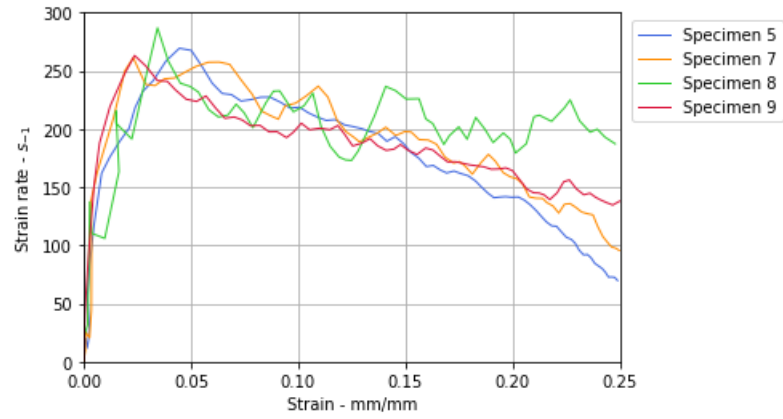
Figure 8.6: Strain rate during the tests
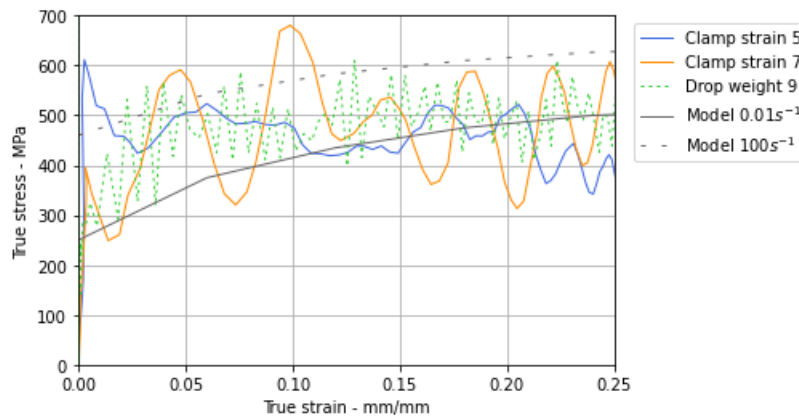
Figure 8.7: Specimen 5 and 7 stress-strain results, compared with the drop weight measurement specimen 9 and material model
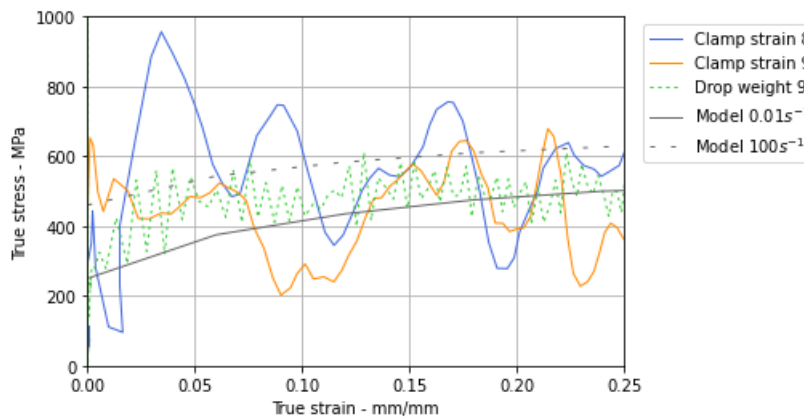
Figure 8.8: Specimen 8 and 9 stress-strain results, compared with the drop weight measurement specimen 9 and material model

Figure 8.9 and 8.10 show stress-strain results for all specimens with bending compensation. The clamp force signals are compensated for bending about the Y-axis. This is done by adding the bending strain to the longitudinal strain. Strain as function of Y-bending is defined as follows. The value for z is half the specimen thickness for strain at the specimen surface. The bending compensation serves as indication of an important source of ringing. Curvature is obtained as follows. The clamp section

has four lines in length direction, as pictured in figure 7.1. These lines can be considered virtual extensometers, each consisting of three points. The third point is added to be able to take the first derivative over two sections. When the first derivative is known at two points, the second derivative can be taken by Forward Euler. This is done per line in length direction per time step.

$$\epsilon_{bend} = -z\frac{\partial^2 z}{\partial x^2} \tag{8.1}$$
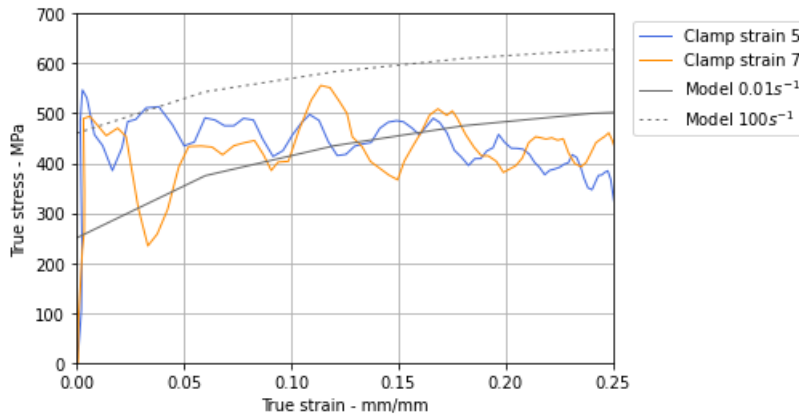
Figure 8.9: Specimen 5 and 7, Y-bending compensation
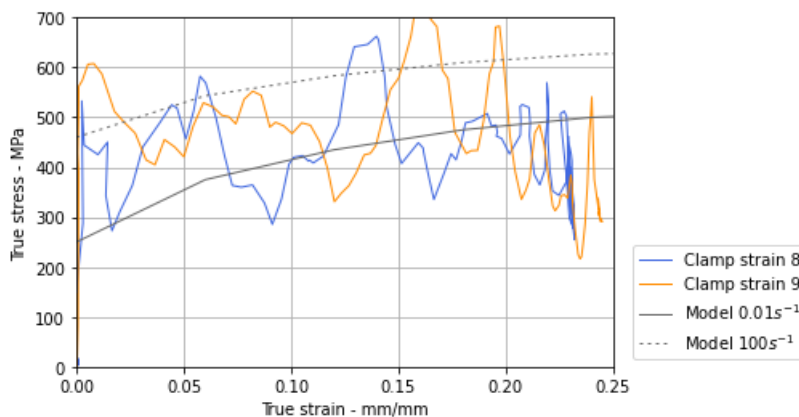
Figure 8.10: Specimen 8 and 9, Y-bending compensation

Lower yield stress results are shown in table 8.2. Bending compensation makes a significant difference for the lower yield stress of specimen 5. However, for the average of all specimens, it does not make a significant difference. Although the drop weight stress-strain results are rough, they are smoothed by taking the time derivatives over several time steps. This time difference smooths the lower yield peak.

Table 8.2: Lower yield stress result per measurement method, averaged from 4 specimens

Method	Lower yield stress - MPa
Average clamp	530
Average clamp - Y-bending compensation	536
Drop weight	300

8.4. Digital image correlation precision

Digital image correlation gives uncertainty intervals per position per time step. Two signals that should be similar, are compared. It is checked whether this similarity is within the presented precision. The case is applied on drop weight rotations as described in chapter 8.2. From three points on the drop weight, z-rotation r_z is determined as $r_z = (-\partial y/\partial x)_a = (\partial x/\partial y)_b$. The indices correspond to the line segments in figure 8.3. This can be done as each point has an x, y and z position per time step. Consequently, the numerator from $\partial y/\partial x$ is perturbed by the precision interval, such that the numerator becomes as large as possible. The denominator is perturbed such, that it becomes as small as possible. That gives the three signals as shown in figure 8.11. The two derivatives are close on half the time domain. The maximum deviation between the derivatives is within twice the precision interval of $\partial y/\partial x$. If it is assumed that both derivatives have an equal precision interval, the maximum deviation is lower than the precision interval. The drop weight rotations are small. Differences in drop weight rotations are very small. Therefore, these signals are very sensitive to small perturbations. There are two results from the precision consideration. The first result is that the derivatives match within the precision interval. The second result is that the precision interval is sufficiently small. Therefore, the digital image correlation is considered representative for positions during the test.
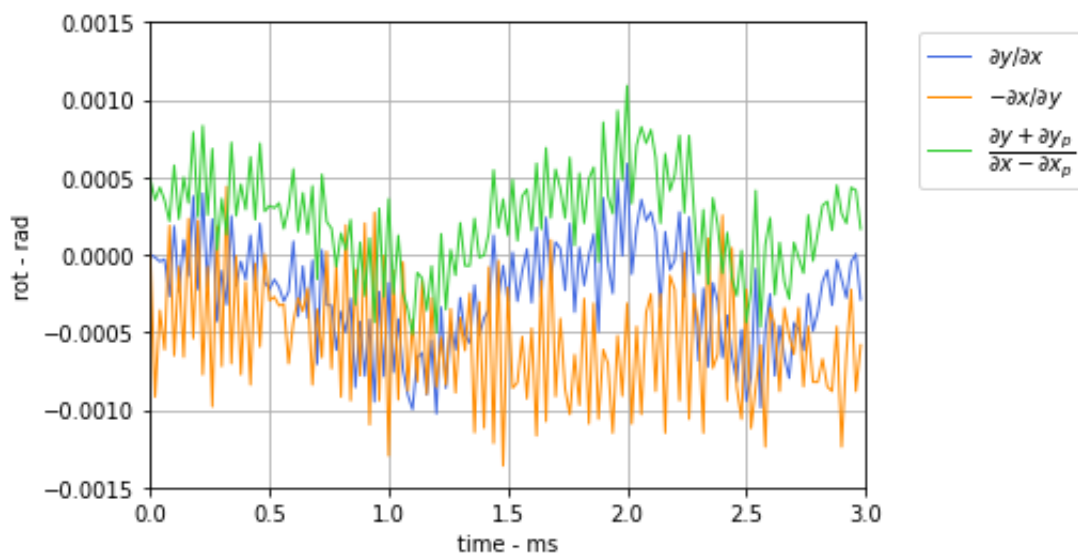
Figure 8.11: Comparison of different derivatives that should equal within precision interval, the z-rotations

9

Discussion

The main question of this thesis is how stress-strain behavior of mild steel can be determined at intermediate strain rates between $100s^{-1}$ and $500s^{-1}$. For answering the question, the main criteria in this thesis are the quality of the measured lower yield stress and plastic tangent modulus. The criteria will be weighed with the amount of ringing that is shown. In the measurements, specimen 5 performs best. It has the least amount of ringing. Specimen 9 has the drop weight acceleration measured. Both stress-strain results are comparable. Especially on strains between 0.02 and 0.2, the signal of specimen 5 and the drop weight signal from specimen 9 oscillate around a comparable value. As the signals come from completely different principles, this result is regarded important. The force signal is a value of a freely falling drop weight. The ringing range in the raw signal of specimen 5 is 20 percent of the stress value. The shape of the stress-strain curve is comparable to mild steel stress-strain curves as obtained by Langseth et al., 1991. The sample rate of the acceleration signal was higher than needed. By reducing the sample rate, resolution is increased. If the clamp section is not measured, 30 mm of the specimen can be measured, rather than the current 60 mm. This reduces measurement errors. This might produce a smoother signal.
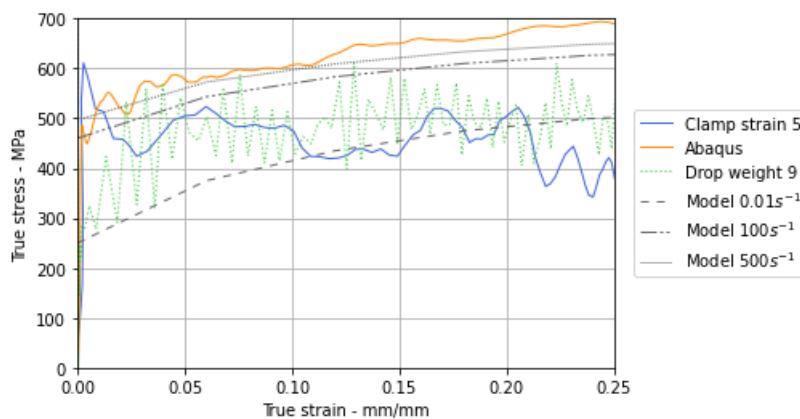
Figure 9.1: Specimen 5 and specimen 9 drop weight

In order to get insight in the amount of bending in ringing, clamp strains are compensated for bending strain. This reduces ringing significantly and also shows where the average of a bending vibration should lie. This procedure is not shown to be used in presented stress-strain curves. Significant bending is present about the Y-axis. This had already been shown in the explicit model. As intended, the clearance between specimen and drop tower was 0.2mm. The clearance is a source of bending. If the drop weight fits exactly inside the specimen before installation in the drop tower, the fit is not always as good after installation. This can result in extra tenths of millimeters clearance. Drop tower motion is not modelled or measured. If the drop tower moves in z-direction, the motion needs to be transferred to the

drop weight via the specimen. This will also create Y-bending. Digital image correlation is a valuable tool in investigating the amount of bending in the specimen.

The drop weight signal shows a low lower yield stress, as the derivative over 16 time steps smooths out the lower yield peak. The position signal is differentiated twice. That is smoothing the force signal. The mentioned camera adjustments avoid smoothing. The clamp strain lower yield stress measurement deviates 25% from the Abaqus model. Even the model shows an oscillation from the lower yield point. The lower yield stress measurement is influenced by a dynamic effect, that also shows up in the model. For better dynamic behavior, the specimen design needs to be adjusted. The lower yield peak is also sensitive for y-bending. This is observed when comparing the lower yield peak from specimen 5 in figure 8.7 and 8.9. Y-bending can be reduced by improving production of the catcher radius and adjusting fixture motion.

10

Conclusion

Two criteria need to be considered to answer the main question of this thesis. The criteria are measurement of the lower yield stress and the plastic tangent modulus. The elastic deformation of the clamp section had been used to obtain the load. This showed reasonable agreement with the load from the drop weight acceleration. Stress-strain behavior of mild steel at strain interval 0.02-0.2mm/mm can be measured by means of a U-shaped specimen and a drop tower, as it is.

Measurements and model showed certain agreement on the lower yield stress peak. At lower yield, there are a dynamic effect in the model and y-bending in the specimen that need improvement. That gives a drop test that can provide stress-strain behavior of mild steel at intermediate strain rates.

A
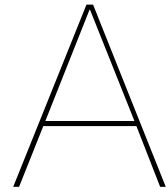
Appendix, Physical model validation

This chapter shows a simple measurement that relates fall energy to strain energy in the specimen. Four specimens have been tested in the drop tower. Fracture is not in the scope of this thesis. Therefore the specimens did not break. Physical deformation was measured after testing. The measurement that has the smallest chance on misreadings, is the measurement where the caliper can be simply put between the shoulders of the specimen. Length measurements as shown in table A.1 were taken before and after the drop test. Both legs of the u-shaped specimen are considered. The first four specimens had an added plastic hinge on the one leg of the specimen only. This side is the front side.

Specimen length between shoulders in mm							
	Before testing				After testing		
Specimen	Front		Back		Front		Back	
	Left	Right	Left	Right	Left	Right	Left	Right
2			19.00	19.00			19.90	19.90
3	19.10	19.05	19.15	19.15	19.85	19.80	20.00	19.90
4	19.15	19.15	19.15	19.15	20.30	20.25	20.40	20.40

Table A.1: Length measurements, before and after testing, initial tests without digital image correlation

Specimen 1 had an elongation of 0.3 mm, measured on at least 2 places, but not stored in detail. The gauge section width had been measured on 3 locations: at the places where the radii end and at the centre. The average width was 4.95 mm with a maximum deviation of 0.10mm. The specimen has a second plastic area that was not modelled in the one dimensional equation. In this way, the displacement during testing is spread over the gauge section and the added plastic hinge. Therefore the front side elongation between shoulders after testing is slightly lower than the back side, as can be seen in the table above. The deformations, shown in table A.2, are obtained as function from drop height. If the simulation runs long enough, elongations can be directly obtained from Abaqus.

Comparison test results and models						
Drop height	Velocity	Elongation physical	Max elongation 1D model	Max elongation Abaqus	Final elongation Abaqus	Relative, Abaqus/physical
cm	m/s	mm	mm	mm	mm	-
5	1.0	0.3	0.47	0.47	0.43	1.43
10	1.4	0.85	0.88	0.88	0.82	0.96
17	1.8	1.25	1.39	1.40	1.34	1.07

Table A.2: Comparison of measurements and calculations, absolute and relative
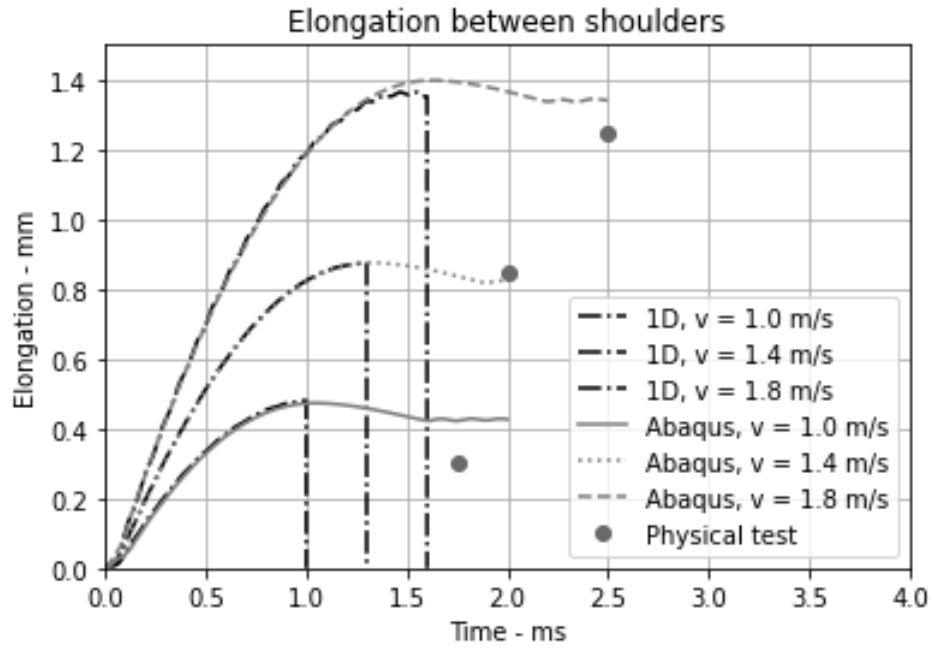
Figure A.1: Comparison of Abaqus, the 1D derivation and physical drop test results

One-dimensional calculations, Abaqus and physical test results are shown in figure A.1. Specimens 2 to 4 show a deviation in final elongation of 7 percent or less. These deviations, together with good agreement between Abaqus results and the one dimensional calculation, indicate that there might not be a significant problem in the calculations. Specimen 1 is over predicted by 43 percent. A measurement error of 0.1 mm already gives this difference between prediction and measurement. However, some specimens have been digitized, which showed the same result as the caliper measurement. Therefore a misreading of the magnitude of 0.1 mm is unlikely. The drop weight might have had too much friction during the first test. Strain energy is more sensitive to lower yield stress than tangent modulus. Therefore, the lower yield stress might have the correct order of magnitude in the current material model.

B

Appendix, Parabolic exponential strain rate sensitivity model

It is common practice that a linear line is fitted through a data set. As can be seen in figure B.1, as the steel gets milder, it shows less linearity on log-log scale over the strain rate domain from quasi-static to 500 per second. The results of the 8 researchers all together form a direction field. The direction field is shown below. The group of researchers is as follows: Huh et al., 2009, Langseth et al., 1991, Jocham et al., 2017, Getter et al., 2015, Singh et al., 2013, Pipard et al., 2013, Xia et al., 2015, Fang, 2021 and Scholl et al., 2018. A family of parabolas is fitted through the direction field.
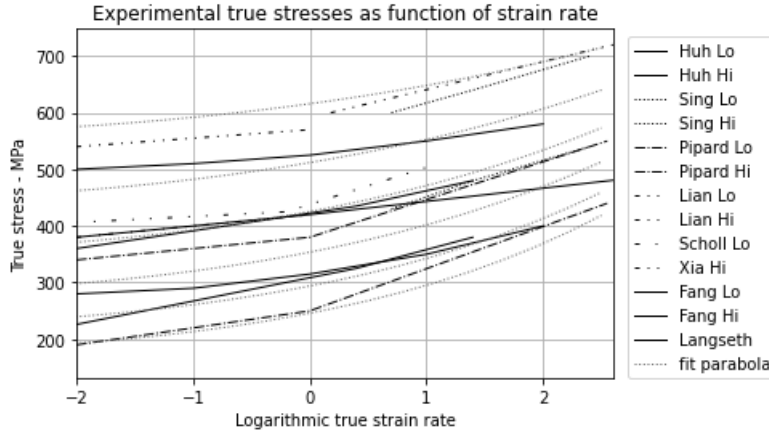
Figure B.1: Results from 8 researchers compared

The family of parabolas on log-log scale is obtained from the equation below. The feature that this equation shows is that higher quasi-static stresses show lower strain rate sensitivity. In other words, high strength steel has less strain rate sensitivity than mild steel. A parabola through the origin is shifted upwards with $\log \sigma_{qs}$, the quasi-static strength. Consequently the graph is shifted left by $\log \dot{\epsilon}_0$, the quasi-static strain rate. A and C are empirical parameters. This equation is referred to as the strain rate sensitivity model in this thesis. The value of C is -0.05. This is valid on loglog domain $\{\sigma, \dot{\epsilon} \mid 2.3 < \sigma_{qs} < 2.8, -4 < \dot{\epsilon} < 2.7\}$.

$$\log \sigma_D = a(\log \dot{\epsilon} - \log \dot{\epsilon}_0)^2 + \log \sigma_{qs} + C \tag{B.1}$$

Where

$$a = \frac{1}{82.2}(-\log \sigma_{qs} + 3) \tag{B.2}$$

The quasi-static result of Huh et al., 2009 for SPRC390E-bh steel is taken as quasi-static stress-strain curve. Figure B.2 shows how quasi-static stress values can be shifted upwards, point by point, dependent on the strain rate. As the strain rate gets higher, hardening decreases. In other words, the tangent modulus gets smaller as strain rate increases. This is the reason that the stress-strain rate model was adopted. With decreasing value of the tangent modulus, intersections with their derivative shift to lower strains. This shift is considerable. According to Considère, necking starts at the intersections.
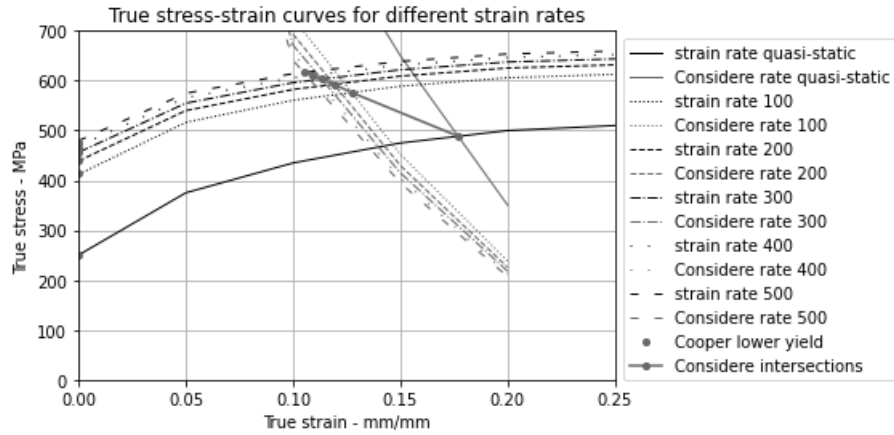
Figure B.2: Strain rate dependent stress-strain curves and crossings with their derivatives

Figure B.2 shows that according to Considère, necking occurs at a decreasing strain with increasing strain rate. This is in accordance with Langseth et al., 1991. Langseth concludes that this is caused by increased heat dissipation with increasing strain rate. Langseth reports a maximum relative decrement of 30 percent of the strain value, where Considère shows a comparable result in this thesis. Although low, the presented necking strain might have the correct order of magnitude.

C
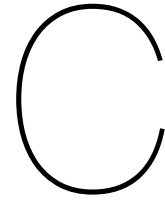
Appendix, Python one-dimensional calculation

The following functions have been created for the one-dimensional calculation. By the end of the code, main function 'oneDfemAllStp' is called with the parameters of the test setup. Adding an extra element for the extra plastic hinge shows that it starts to yield later than the gauge section, if the width is larger than the gauge section width. It has been checked whether it is also allowed to take one effective gauge length for both plastically deforming areas. Python 3.8 has been used in Spyder 4.
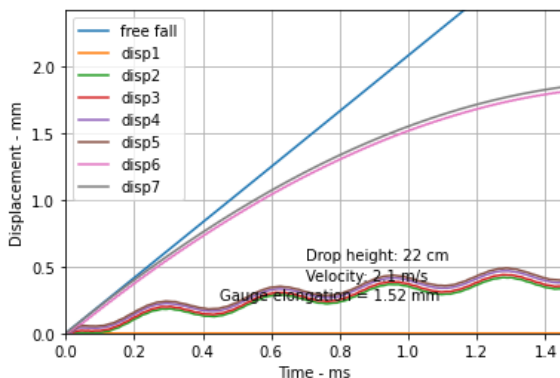
(a) Nodal displacements, 6 elements
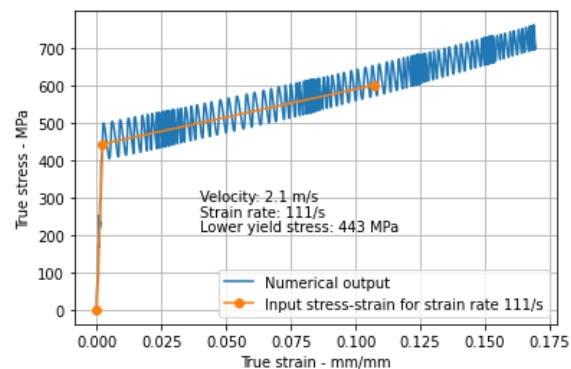
(b) Comparison of stress-strain curves

```python
# -*- coding: utf-8 -*-
import numpy as np
import matplotlib.pyplot as plt
import numpy.linalg  as npl


def Xderivative(nDof,nel,dXshift,grav,Kstiff,MassMtx1,X):
    DampVal = 0.5
    Damp=np.eye(nDof)*DampVal
    mtx=np.zeros((2*nDof,2*nDof))
    mtx[0:nDof,nDof:2*nDof]=np.eye(nDof)
    mtx[nDof:2*nDof,0:nDof]=-np.matmul(MassMtx1,Kstiff)
    mtx[nDof:2*nDof,nDof:2*nDof]=-np.matmul(MassMtx1,Damp)
    gravV=np.zeros(2*nDof)
    gravV[2*nDof-1]=grav
    dX=np.matmul(mtx,X) + dXshift + gravV
    return dX
```

```python
def Rungekutta4(nDof,nel,dTime,dXshift,grav,Kstiff,MassMtx1,X):
    rkDiv=np.zeros((X.size,4))
    for rkC in range(0,4):
        extras=rkDiv[:,rkC-1]*   int(0.5*(rkC+1))/2
        rkDiv[:,rkC] = dTime * Xderivative(nDof,nel,dXshift,grav,Kstiff,
                                           MassMtx1,X+extras)
    X+=(rkDiv[:,0] + 2*rkDiv[:,1] + 2*rkDiv[:,2] + rkDiv[:,3]  )/6
    return X


def stiffnessMatrix(nDof,nel,widths,lengths,tGauge,Emods):
    Kstiff=np.zeros((nDof,nDof))
    for eCt in range(0,widths.size):
        kEl=Emods[eCt]*widths[eCt]*tGauge/lengths[eCt]*np.array([[1,-1],[-
1,1]])
        Kstiff[eCt:eCt+2,eCt:eCt+2]+=kEl
    return Kstiff


def TrueSigmaStp(widths,lengths,tGauge,X,dX,dTime,mass,trueStrainm1):
    nel = int(lengths.size)
    nDof=nel+1
    lengthT=np.zeros(nel)
    DtrueStrainStp =np.zeros(nel)
    trueStrainStp =np.zeros(nel)
    trueSigmaStp =np.zeros(nel)
    for elC in range(0,nel):
        lengthT[elC]=X[elC+1]-X[elC] + lengths[elC]
        trueStrainStp[elC] = np.log(lengthT[elC] /lengths[elC])
        DtrueStrainStp[elC] = (trueStrainStp[elC]-trueStrainm1[elC])/dTime
        areaT = lengths[elC]*widths[elC]*tGauge/lengthT[elC]
        force=dX[nDof*2-1]*mass
        trueSigmaStp[elC] = force/areaT
    return force,DtrueStrainStp,trueSigmaStp,trueStrainStp


def shiftToPlastic(nDof,nel,emods,elCf,widths,lengths,tGauge,Emod,EmodTe,
                   schakelStep,trueSigma,lowerYield,lyPass,tSt,dXshift,grav,
                   MassMtx1,X,dX):
    dXnew=np.zeros(nDof*2)
    KstiffRed=stiffnessMatrix(nDof,nel,widths,lengths,tGauge,emods)
    if abs(trueSigma) > abs(lowerYield[elCf]):
        lyPass[elCf]=1
        schakelStep[elCf]=int(tSt)
        emods[elCf]=EmodTe
        KstiffRed=stiffnessMatrix(nDof,nel,widths,lengths,tGauge,emods)
        dXnew=Xderivative(nDof,nel,dXshift,grav,KstiffRed,MassMtx1,X)
        dXshift[nDof+elCf : nDof+elCf+2]-=dXnew[nDof+elCf : nDof+elCf+2]

    return emods,KstiffRed,lyPass,schakelStep,dXnew,dXshift


def FangQsToDyn(qsStress,rate):
    fanX=np.array([-2,2])
```

```python
    fanYloSig=np.array([160,400])
    fanYhiSig=np.array([310,500])
    slopeLo=(fanYloSig[1] - fanYloSig[0]) / (fanX[1] - fanX[0])
    slopeHi=(fanYhiSig[1] - fanYhiSig[0]) / (fanX[1] - fanX[0])
    dSlopDy=(slopeHi-slopeLo)/( fanYhiSig[0] - fanYloSig[0])
    dy=qsStress-fanYloSig[0]
    slope=dy*dSlopDy+slopeLo
    dx=rate-fanX[0]
    fanYfun=np.array([qsStress,qsStress+slope*dx])
    return fanYfun



def oneDfemAllStp(nDof,nel,Emod,EmodTe,widths,lengths,tGauge,dTime,grav,mass,
                  MassMtx1,nstep,time,X):
    trueStrain    = np.zeros((nstep+1,nel))
    DtrueStrain   = np.zeros((nstep+1,nel))
    DtrueStrainAvg  = np.zeros((nstep+1,nel))
    lengthT       = np.zeros((nstep+1,nel))
    trueSigma     = np.zeros((nstep+1,nel))
    force         = np.zeros(nstep+1)
    dispAll       = np.zeros((nDof,nstep+1))
    schakelStep   = nstep * np.ones(nel)

    lyPass=np.zeros(nel)
    lowerYield=np.zeros(nel)
    dXshift = np.zeros(2*nDof)
    emods=Emod * np.ones(nel)
    Kstiff=stiffnessMatrix(nDof,nel,widths,lengths,tGauge,emods)
    for tSt in range(1,nstep):
        dX=Xderivative(nDof,nel,dXshift,grav,Kstiff,MassMtx1,X)
        X = Rungekutta4(nDof,nel,dTime,dXshift,grav,Kstiff,MassMtx1,X)
        X[0]=0.
        force[tSt],DtrueStrain[tSt,:],trueSigma[tSt,:],trueStrain[tSt,:]= \
         TrueSigmaStp(widths,lengths,tGauge,X,dX,dTime,mass,trueStrain[tSt-
1,:])

        for elCf in range(0,nel):
            rateC=trueStrain[tSt,elCf]/time[tSt]
            if lyPass[elCf]==0 and rateC>1.:
             dynStress=FangQsToDyn(250,np.log10(trueStrain[tSt,elCf]/time[tSt]))
              lowerYield[elCf]=dynStress[1]*1e6  # dynstress was al een vector
            emods,Kstiff,lyPass,schakelStep,dXnew,dXshift=shiftToPlastic(nDof,
                    nel,emods,elCf,widths,lengths,
                  tGauge,Emod,EmodTe,schakelStep,trueSigma[tSt,elCf],    \
                   lowerYield,lyPass,tSt,dXshift,grav,MassMtx1,X,dX)

            if tSt==int(schakelStep[nel-2]+1):
                print('LY ',lowerYield*1e-6)
                print('rate',DtrueStrainAvg[int(schakelStep[nel-2]-1)])

         # print status
        if tSt==int(nstep/100) or tSt==int(nstep/20) or tSt==int(nstep/10) \
         or tSt==int(nstep/5) or tSt==int(nstep/2):
            print(100*tSt/nstep,'% of steps done')

        DtrueStrainAvg[tSt] = trueStrain[tSt]/time[tSt]
```

```
        dispAll[:,tSt]=X[0:nDof]
    return dispAll,DtrueStrain,DtrueStrainAvg,lowerYield,schakelStep,  \
                trueStrain,trueSigma


widths=0.001*np.array([6,    15,15,15,    5,    25])
lengths=0.001*np.array([2.3,    20,30,20,    7.66,    60])

gaugeEl=4
Emod=210e3
rho=7800

fallH=0.22
mass=4.5

nstep=int(1e4)
Ttime=np.zeros((1,int(nstep+1)))

tEnd=0.0015
time=np.linspace(0,tEnd,nstep+1)
dTime=time[1]-time[0]

tGauge=0.001*2 #m
Emod=210*1e9 #N/m2
EmodTe= 96.7*1e6/0.105
EmodT= 150*1e6/0.1#140*1e6/0.11

grav=9.81#/100    #m/s2
tInit=np.sqrt(2*fallH/grav)
vInit=grav*tInit

nDof=lengths.size+1
nel=lengths.size

massVec=np.ones(nDof)
massVec[1:nDof]=rho*tGauge*widths*lengths
massVec[nDof-1]+=mass
MassMtx=np.diag(massVec)
MassMtx1=npl.inv(MassMtx)

X            = np.zeros(nDof*2)
X[2*nDof-1]        += vInit

dispAl,DtruStn,DtruStnA,loYiel,shiftR,truStn,truSig= oneDfemAllStp(nDof,
  nel,Emod,EmodTe,widths,lengths,tGauge,dTime,grav,mass,MassMtx1,nstep,time,X)
```

Bibliography

Abaqus. (2017). Abaqus manual. https://abaqus-docs.mit.edu/2017/English/SIMACAEBMKRefMap/ simabmk-c-linbending.htm#simabmk-c-linbending-t-FurtherExamples-sma-topic14

Bhujangrao, T., Froustey, C., Iriondo, E., Veiga, F., & Darnis, F., P.and Mata. (2020). Review of intermediate strain rate testing devices. *Metals*, *10*, 894. https://doi.org/10.3390/met10070894

Broekhuis, G. (2020). Design guide for stress-strain measurements of strain rate sensitive metals using impact experiments and dic. *MsC Thesis, Delft University of Technology.*

Chan, J. (2009). Design of fixtures and specimens for high strain-rate tensile testing on a drop tower. *BsC Thesis, Massachusetts Institute of Technology*.

Cowper, G. R., & Symonds, P. S. (1957). *Strain-hardening and strain-rate effects in the impact loading of cantilever beams* (tech. rep.). Brown Univ Providence Ri.

Fang, X. (2021). Oscillation-free determination of material properties at high strain rate. *Forming the future, conference paper*. https://doi.org/10.1007/978-3-030-75381-8.

Getter, D., Kantrales, G., G.R., C., Eudy, S., & Fallaha, S. (2015). Strain rate sensitive steel constitutive models for finite element analysis of vessel-structure impacts. *Marine Structures*, *44*, 171–202. https://doi.org/10.1016/j.marstruc.2015.09.001

Huh, H., Lim, J.H., & Park, S. (2009). High speed tensile test of steel sheets for the stress-strain curve at the intermediate strain rate. *International Journal of Automotive Technology*, *10*(2), 195–204. https://doi.org/10.1007/s12239-009-0023-3

Jocham, D., Norz, R., & Volk, W. (2017). Strain rate sensitivity of dc06 for high strains under biaxial stress in hydraulic bulge test and under uniaxial stress in tensile test. *International Journal of Material Forming*, *10*, 453–461. https://doi.org/10.1007/s12289-016-1293-8

Kolsky, H. (1964). Stress waves in solids. *Journal of Sound and Vibration*, *1*, 88–110. https://doi.org/ 10.1016/0022-460X(64)90008-2

Langseth, M., Lindholm, U., Larsen, P., & Lian, B. (1991). Strain-rate sensitivity of mild steel grade st52-3n. *Journal of Engineering Mechanics*, *117*(4), 719–732. https://doi.org/10.1061/(ASCE)0733-9399(1991)117:4(719)

Perogamvros, N., Mitropoulos, T., & Lampeas, G. (2016). Drop tower adaptation for medium strain rate tensile testing. *Experimental Mechanics*, *56*, 419–436. https://doi.org/10.1007/s11340-015-0112-3

Pipard, J., Balan, T., Abed-Meraim, F., & Lemoine, X. (2013). Elasto-visco-plastic modeling of mild steels for sheet forming applications over a large range of strain rates. *International Journal of Solids and Structures*, *50*, 2691–2700. https://doi.org/10.1016/j.ijsolstr.2013.04.022

Reedlunn, B., Daly, S., Hector, L. J., Zavattieri, P., & Shaw, J. (2013). Tips and tricks for characterizing shape memory wire part 5: Full-field strain measurement by digital image correlation. *Experimental Techniques*, *37*, 62–78. https://doi.org/10.1111/j.1747-1567.2011.00717.x

Scholl, N., Minuth-Hadi, F., & Thiele, K. (2018). Modelling the strain rate dependent hardening of constructional steel using semi-empirical models. *Journal of Constructional Steel Research*, *145*, 414–424.

Schutte, J., Dannenberg, J., Wijnant, Y. H., & de Boer, A. (2010). An implicit and explicit solver for contact problems. *Proceedings of ISMA2010 including USD2010*, 4081–4094.

Singh, N., Cadoni, E., Singha, M., & Gupta, N. (2013). Dynamic tensile and compressive behaviors of mild steel at wide range of strain rates. *Journal of Engineering Mechanics*, *139*(9), 1197–1206. https://doi.org/10.1061/(ASCE)EM.1943-7889.0000557

Xia, Y., Zhu, J., Wang, K., & Zhou, Q. (2016). Design and verification of a strain gauge based load sensor for medium-speed dynamic tests with a hydraulic test machine. *International Journal of Impact Engineering*, *88*, 139–152. https://doi.org/10.1016/j.ijimpeng.2015.10.004

Xia, Y., Zhu, J., & Zhou, Q. (2015). Verification of a multiple-machine program for material testing from quasi-static to high strain-rate. *International Journal of Impact Engineering*, *86*, 284–294. https: //doi.org/DOI10.1016/j.ijimpeng.2015.07.010

Zhu, D., Rajan, S., Mobasher, B., Peled, A., & Mignolet, M. (2011). Modal analysis of a servo-hydraulic high speed machine and its application to dynamic tensile testing at an intermediate strain rate. *Experimental Mechanics*, *51*, 1347–1363. https://doi.org/10.1007/s11340-010-9443-2